Winter 12-15-2022

Quasiparticle and Excitonic Effects in Two-Dimensional van der Waals Materials

Linghan Zhu
Washington University in St. Louis

WASHINGTON UNIVERSITY IN ST. LOUIS

Department of Physics

Dissertation Examination Committee:
Li Yang, Chair
Erik Henriksen
Rohan Mishra
Sheng Ran
Alexander Seidel

Quasiparticle and Excitonic Effects in Two-Dimensional van der Waals Materials

by

Linghan Zhu

A dissertation presented to
Washington University in St. Louis
in partial fulfillment of the
requirements for the degree
of Doctor of Philosophy

December 2022
St. Louis, Missouri

Table of Contents

Acknowledgements

I would like to express my sincere gratitude to my thesis advisor, Prof. Li Yang, for being a wise and insightful advisor who patiently guides me through the journey towards a condensed matter physicist. He always comes up with novel ideas about where the research goes, and has a macroscopic view of the whole physics picture while not losing attention to every detail. I appreciate particularly his critical praises and criticisms, which helped me reckon on how I could improve and grow both as a researcher and as a mature person.

Throughout my graduate study, other faculty members in the physics department have also helped me from different perspectives. I am impressed by the instructions from Prof. Carl Bender, Prof. Zohar Nussinov, Prof. Anders E. Carlsson, and Prof. Saori Pastore. I am deeply grateful to Prof. Willem H. Dickhoff, who introduced the wonder world of many-body theory to me. I felt pleasured to be his teaching assistant for Introduction to Quantum Physics. Being able to give lectures and design homework has been a precious experience to me, which reminds me of my undergraduate study and how I decided to continue learning physics in graduate school. I am also thankful to my committee members, Prof. Alexander Seidel, Prof. Erik Henriksen, Prof. Sheng Ran, and Prof. Rohan Mishra, for witnessing my progress towards the fulfillment of my research.

I would like to express my thanks to the previous and current group members, Dr. Yufeng Liang, Dr. Ruixiang Fei, Dr. Shiyuan Gao, Dr. Wenshen Song, Dr. Xiaobo Lu, Du Li, Haonan Wang, Yizhou Wang, for helping me with my research and being my true friends. I am also appreciative of the companionship from Dr. Ji Xia and Yashika Kapoor. I would always remember the splendid sunsets we witnessed every time we got out of the gym after a sweaty workout.

My special thanks go to Yimo Zhang, who has led me to a magnificent new world, and helped me become who I am. I always hope he could freely pursue what satisfies him.

I am humbled to have some long-term friends that I would cherish for life. I would like to thank Gege Guang for always being by my side. She has a magic way to reassure me and teach me to enjoy a light-hearted life, which helped me go through all the dark moments. I would also thank Dr. Yu Hu for sharing his happiness and sorrow with me, and always ready to listen to my complaints and pull me out from misgivings. I do not usually take the initiative to talk to my friends, but for sure I appreciate their patience to tame me.

I am deeply indebted to my parents for their love. They have been supportive to every decision I made, and respectful of my opinions. I also miss my grandparents who are in heaven. Hope I have grown up to be your pride.

Lastly, thank the stubborn little girl who never gives up on her dreams. I have always been, and I will always be.

Linghan Zhu

Washington University in St. Louis

December 2022

Dedicated to those who are pursuing their dreams.

ABSTRACT OF THE DISSERTATION

Quasiparticle and Excitonic Effects in Two-Dimensional van der Waals Materials

by

Linghan Zhu

Doctor of Philosophy in Physics

Washington University in St. Louis, 2022

Professor Li Yang, Chair

Since their discovery, low dimensional van der Waals materials have attracted increasing research interests. They serve as ideal platforms to study novel physics in reduced-dimensional systems, and are critical in nowadays' nanotechnology applications. Due to the reduced dielectric screening in low dimensions, strong excited state properties dictate their electronic, transport and optical properties, the study of which calls for a description of the many-particle interactions beyond the traditional density functional theory. This is where the many-body perturbation theory comes into play. In this thesis, I will present a comprehensive study of the quasiparticle and excitonic properties of a variety of two-dimensional materials using first-principles simulations with many-body effects taken into consideration.

In Chapter 3, we study the phonon assisted optical excitations in monolayer MoS_2 and MoS_2/WS_2 heterostructures. The monolayer MoS_2 was shown experimentally to possess a direct band gap, whereas its bilayer form characterizes an indirect band gap. The energy difference between the valence band maximum at Γ and K is small, motivating us to study the possibility of brightening the indirect exciton states with the assistance of acoustic phonons. Since photon cannot provide momentum in optical transitions, an elementary excitation that has finite

momentum is needed to assist the brightening of a momentum dark exciton. Our results not only confirm the increased oscillator strength of originally forbidden indirect exciton states, but also help identify certain phonon branches that are capable of fulfilling this process.

In Chapter 4, we turn to the study of a correlated magnetic two-dimensional material, $CrCl_3$. Due to the localized 3d orbitals of the magnetic atom Cr, its electronic band structure features flat bands around the Fermi level. The flat bands warrant large joint density of states in the system, which is promising for strong excitonic effects. We show that the exciton binding energy in monolayer $CrCl_3$ is much larger than typical two-dimensional materials, and we further find that the exciton binding energy in bulk $CrCl_3$ remains large due to the unique flat bands in the magnetic material. The crystallographic structure and magnetic order dependence of the excitonic effects are also studied in bilayer $CrCl_3$.

In Chapter 5, the quasiparticle-plasmon coupling in doped moiré heterostructure MoS_2/WS_2 is investigated. Under electron doping, the different local stackings in a moiré system renders varied strength of quasiparticle-plasmon couplings. This in turn modifies the original moiré potential landscape and results in increased moiré potential. Since the physical properties of a moiré structure are largely determined by the moiré potential, the doped moiré system experiences much stronger correlated effects and features a set of ultra-flat minibands. A quantum phase transition between the Mott and charge-transfer insulating states at half-filling is also examined, which helps us understand the rich insulating states observed in gated transition metal dichalcogenides moiré systems in recent experiments.

Chapter 1: Introduction

1.1 Low dimensional van der Waals materials

The successful exfoliation of monolayer graphene has opened the new era of studies of low-dimensional materials [1]. According to a simple tight binding model, the high symmetric honeycomb lattice leads to a linear-dispersed electronic band structure at the K point, which boasts the massless Dirac fermions in graphene [2–4]. There are two carbon atoms in a unit cell, each forming a triangular sublattice in monolayer graphene. Considering hopping only between nearest neighbors, and on-site energy being zero, the real space Hamiltonians for the nearest unit cells read $H(\mathbf{0}) = \begin{pmatrix} 0 & 1 \\ 1 & 0 \end{pmatrix}$, $H(\boldsymbol{a}_2) = H(\boldsymbol{a}_2 - \boldsymbol{a}_1) = \begin{pmatrix} 0 & 1 \\ 0 & 0 \end{pmatrix}$, $H(-\boldsymbol{a}_2) = H(\boldsymbol{a}_1 - \boldsymbol{a}_2) = \begin{pmatrix} 0 & 0 \\ 1 & 0 \end{pmatrix}$. The Fourier transform of the Hamiltonian to reciprocal space $H_k = \sum_{\boldsymbol{k}} e^{i\boldsymbol{k}\cdot\boldsymbol{R}} H^{ij}(\boldsymbol{R})$, $H_k^0 = t\begin{pmatrix} 0 & h_k \\ h_k^* & 0 \end{pmatrix}$ where $h(\boldsymbol{k}) = 1 + e^{i\boldsymbol{k}\cdot\boldsymbol{a_2}} + e^{i\boldsymbol{k}\cdot(\boldsymbol{a_2}-\boldsymbol{a_1})}$, yields the electronic band structure of monolayer graphene $\varepsilon_{\pm}(\boldsymbol{k}) = \pm t|h_k|$, as shown in Figure 1.1 (b). The resulting eigenvalues at high symmetry points are therefore $\varepsilon_{\pm}(\Gamma) = \pm 3t$, $\varepsilon_{\pm}(M) = \pm t$, $\varepsilon_{\pm}(K) = 0$.

Together with the reduced dielectric screening in low dimensions, the carrier mobility in graphene is high, leading to applications of graphene in integrated circuit devices, light-emitting diodes [5,6], etc. Despite the vast electronic applications of graphene, the gapless Dirac cone has inhibited its optical responses, and a search for strong photoluminescence semiconductor is due.

When the sublattice degeneracy in monolayer graphene is broken, a finite band gap naturally arises at K. If the potential difference between the two sublattices is 2μ, then the Hamiltonian

becomes $H_k = H_k^0 + \begin{pmatrix} \mu & 0 \\ 0 & -\mu \end{pmatrix}$, and the degeneracy at K is broken $\varepsilon_{\pm}(K) = \pm\mu$. Monolayer hexagonal boron nitride (hBN) falls into this category. Its lattice structure is the same as graphene, despite that each unit cell contains one boron and one nitride atoms. The broken sublattice degeneracy renders a direct band gap at $K \sim 7eV$ in monolayer hBN. Whereas the hBN crystal is an indirect band gap semiconductor [7]. Previous optical spectroscopy measurements have demonstrated phonon assisted bright optical transitions in bulk hBN [8]. The large band gap in hBN has triggered wide interests in deep ultraviolet (DUV) optoelectronic applications [9,10].

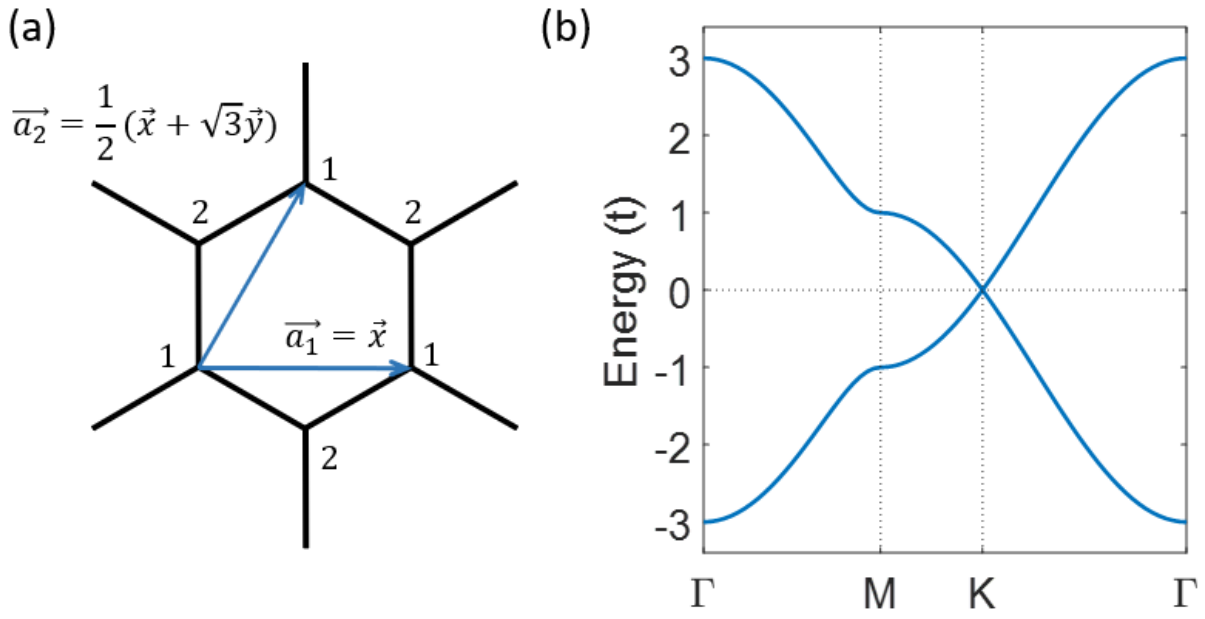

Figure 1.1 (a) Hexagonal lattice structure of graphene. The unit cell is composed of two carbon atoms, which constitutes two triangular sublattices. (b) Tight-binding calculated band structure of graphene, featuring zero gap and a linear-dispersed band at the K point.

More recently, the transition metal dichalcogenides (TMD) family has emerged as a promising platform for visible light optical applications. The demonstration of layer dependent photoluminescence spectra in molybdenum disulfide (MoS_2) has revealed the indirect to direct band gap crossover from few-layer to monolayer MoS_2 [11]. In its bulk from, the photoluminescence is quenched due to the indirect nature of the band gap. It is only until exfoliated to monolayer that the band gap becomes direct at K, and significant photoluminescence signal is observed. More interestingly, due to the broken inversion symmetry and spin orbit coupling (SOC), monolayer MoS_2 hosts coupled spin and valley physics, making it an ideal playground for studying the valleytronics [12,13]. Other variants in the TMD family hold similar band structures and properties, and are gaining increasing attentions.

The discovery of ferromagnetism in monolayer $CrGeTe_3$ marks another milestone in the study of 2D van der Waals (vdW) semiconductors [14]. This directly contradicts the Mermin-Wagner theorem [15], which states that the continuous symmetries cannot be spontaneously broken at finite temperature in systems with dimensions $d \leq 2$. However, the strong exchange interaction of density of states (DOS) around the Fermi level allows for the Stoner criterion [16], which stabilizes the ferromagnetism in 2D systems. In 2D ferromagnetic semiconductors, the bands around the Fermi level are typically composed of highly correlated and localized 3d orbitals of the magnetic metals, resulting in small band dispersions. The parallel band dispersion around the band edges results in large joint density of states (JDOS), which promises strong optical transitions. The chromium trihalides family is a group of intralayer FM materials known to possess flat band edges [17]. Depending on the halide species, the interlayer magnetism can be either FM ($CrI3$) or AFM ($CrCl_3$), and the strength of SOC determines the type of magnetic exchange interactions, which could be Ising like (CrI_3) or Heisenberg like ($CrCl_3$). The diversity

within chromium trihalides family warrants its importance in 2D magnetic materials. The class of 2D magnetic semiconductors serves as a building block in the study of spintronics and its applications.

The variety of vdW materials makes it possible to stack different systems together to form more intriguing platforms, also known as homo/hetero structures. Another freedom in the stacked vdW systems is the twist angle between constituent layers. Since the discovery of superconductivity and correlated insulating states in magic angle twisted bilayer graphene [18,19], moiré systems formed by a rotational misalignment or lattice mismatch between semiconducting vdW layers have ignited increasing interests. The moiré supercell allows for the formation of moiré flat bands and mimic of the Wigner crystals [20,21]. The long period moiré potential can contain trapped moiré excitons for higher single photon emission purity and longer exitonic lifetime [22]. These observations established vdW moiré systems as ideal platforms to study highly correlated physics and quantum information applications.

1.2 First principles study of excited state properties

On a theoretical perspective of view, the aforementioned electronic band structures and optical responses in 2D systems are based on various elementary excitations upon external pumps. The precise determination of band edges requires the excitation of an electron quasiparticle from the valence band and a hole quasiparticle from the conduction band. These are, however, single particle excitations that can be approximately described by an independent electron/hole moving in a background potential. When an electron is ejected from the valence band by incident photons, and the Coulomb interaction between the electron and the hole left in the valence band is not screened by the dielectric background, an exciton is formed, which determines the

absorption spectra of the system. The description of exciton therefore requires solving the many-body interactions, as its formation is a two-particle process.

The dielectric screening is weak in systems with reduced dimensions, which dramatically enhances the many-body interactions that are determined by Coulomb interactions. On the other hand, exciton states are a coherent superposition of many similar energy electron-hole pair excitations. Therefore, large exciton binding energies are typically found in low-dimensional materials and can be expected from flat-band materials. The main topic of this thesis will be around the quasiparticle and exciton excitations in low dimensional semiconductors.

I will present a theoretical study of the many-body interactions in a variety of novel 2D materials, which are promising candidates for optoelectronic applications. The study is based on first principles methodologies, which is self-consistent and requires no parameters from experiments. The ground state properties are simulated by density functional theory (DFT) [23,24], which produces reliable crystal structures and non-interacting electronic wavefunctions. As a ground state theory though, DFT is notoriously known to underestimate the electronic band gap and ignore electron-electron interacting dielectric effect. In order to account for the quasiparticle excitations, a theory beyond DFT is needed. For example, even though monolayer MoS_2 is experimentally determined to be a direct gap material [11], it is not until beyond DFT that the correct band alignment is predicted [25]. Within the many-body perturbation theory (MBPT), the quasiparticle self-energy is calculated with GW approximation [26]. G represents the Green's function, and W is the screened Coulomb interaction. The self-energy is directly calculated by their product $\Sigma = GW$, which represents the motion of an electron in the screened background of other electrons. The two-body excitonic effect is calculated with Bethe-Salpeter equation (BSE) [27]. The electron-hole kernel describes

the interaction between electron and hole, which is consisted of two parts, the direct kernel K^d and exchange kernel K^x. The eigenvalues and eigenvectors of the BSE represent the exciton energy and wavefunctions, respectively.

1.3 Outline of the thesis

Based on the first principles techniques, in this thesis, the exciton-phonon interaction is studied in monolayer and bilayer MoS_2. Since the valence band maximum (VBM) at Γ and K are close in energy, the indirect optical transition from valence band at Γ to conduction band at K can be fulfilled by assistance of certain phonon modes. Then I will demonstrate strong excitonic effects in magnetic $CrCl_3$, which has flat bands around the Fermi level. The excitonic effect is predicted to be strong even in the bulk structure, due to its unique band structure. The effect of Hubbard potential in the DFT starting point is also discussed. Finally, the doping effect in twisted MoS_2/WS_2 moiré heterostructure is studied. The quasiparticle-plasmon coupling will substantially deepen the moiré potential and enhance the correlated effect in the moiré system, resulting in ultra-flat bands. The transition between Mott and charge-transfer insulating states at half-filling of the moiré superlattice is discussed.

Chapter 2: Theoretical Framework

The lattice structure and electronic properties of condensed matter systems are largely determined by the outer valence electrons of the constituent atoms. The many-body system is too complicated that an exact solution would be impractical. The electronic Hamiltonian can be treated as independent electrons moving in an effective mean field of the ions and other electrons, then the many-body problem is transformed to a one-particle problem [28–30].

$$\left(-\frac{\hbar^2}{2m}\nabla^2 + V(r)\right)\psi(r) = \varepsilon\psi(r) \tag{2.1}$$

$$H = \sum_i \frac{p_i^2}{2m} + \sum_i v(r_i) + \frac{1}{2}\sum_{i\neq j}\frac{e^2}{|r_i - r_j|} \tag{2.2}$$

The second term covers the electron-ion interaction in the crystal and the external potentials. The third term is the electron-electron interaction. Different ways of approximating the electron-electron interaction have led to different solutions to the one-particle problem.

Central to the first principles studies of the electronic properties of condensed matter systems is the density functional theory (DFT) [23,24]. It is exact in describing the ground state properties, such as total energy and electron charge density distributions, of interacting many-electron systems.

Hartree-Fock approximation, on the other hand, is a variational approach for the ground-state energies and wavefunctions. Because of the variational method, it is not exact compared with DFT.

The excited state properties involve the excitation of particles above the ground state, and need more advanced theoretical treatment beyond DFT. For single particle excitations, GW

approximation is widely adopted to obtain the accurate quasiparticle energies [26,31], and is based on the interacting-particle Green's functions. The description of optical excitations requires the inclusion of electron-hole interactions, and the Bethe-Salpeter equation is generally employed to study the excitonic effects [27].

I will introduce the above-mentioned methodologies for first principles calculations of condensed matter systems in this chapter.

2.1 Density functional theory

2.1.1 Hohenberg-Kohn theorems

The formalism of DFT is based on the theorems proposed by Hohenberg and Kohn in 1964 [23], which states that the ground state energy E of an interacting many-electron system in an external potential $v(r)$ can be expressed as a functional of the charge density ρ. $E[\rho] = \int v(r)\rho(r)dr + F[\rho]$, where $F[\rho]$ is a universal functional of the density, independent of the external potential $v(r)$. This substantially simplifies the N-body problem with $3N$ dimensional wavefunctions $E[\Psi(r_1, .., r_N)]$ to $E[\rho(r)]$. The universality of the energy functional is derived by a proof by contradiction.

The second Hohenberg-Kohn theorem states that the total energy E is a minimum for the correct charge density ρ. This can be proven by a variational principle of quantum mechanics, where the energy of the system is at its minimum for the ground-state wavefunction relative to a small perturbation.

The interacting many-electron system would be exactly solvable if the density functional of external potential $F[\rho]$ were known.

2.1.2 The Kohn-Sham equations

Even though the explicit expression for the density functional is unknown, we can write out analytical contributions that are already known

$$E[\rho] = \int v(r)\rho(r)dr + T[\rho] + \frac{1}{2}e^2 \int \frac{\rho(r)\rho(r')}{|r-r'|} drdr' + E_{xc}[\rho]. \quad (2.3)$$

$T[\rho]$ represents the kinetic energy of the system, and the third term on the right-hand side is the electron-electron interaction in the Hartree approximation. The exchange-correlation energy functional now absorbs the unknown part of DFT. In order to arrive at a practical approach, Kohn-Sham framework further considers a fictitious system with non-interacting electrons in an effective one-body potential. Using the variational principle, the electron density in the non-interacting system is varied to find out the energy minimum of the energy functional of the real interacting system. Then the set of Kohn-Sham equations for the non-interacting system is written [24]

$$\left\{\frac{p^2}{2m} + v(r) + v_H(r) + v_{xc}(r)\right\}\varphi_i(r) = \epsilon_i\varphi_i(r). \quad (2.4)$$

The exchange-correlation potential $v_{xc}(r) = \frac{\delta E_{xc}}{\delta\rho(r)}$ is not known, but there are different approximations for $E_{xc} = \int \rho(r)\varepsilon_{xc}(r)dr$. The exchange-correlation energy density $\varepsilon_{xc}(r)$ is presumed to be a function of local density $\rho(r)$ in the local density approximation (LDA), and a function of $\rho(r)$ and $\nabla\rho(r)$ in the generalized gradient approximation (GGA) [32–34]. These two approximations are developed from charge densities of the homogeneous electron gas, and

are proved to produce accurate ground state properties such as total energy, structural and vibrational properties of a variety of materials.

However, due to the variational construct of the Kohn-Sham equations, the eigenvalues cannot be interpreted as the excitation energies of quasiparticles and do not agree with experimental results. This leads to the notorious underestimate of band gap in DFT. Nonetheless, DFT serves as a good starting point for excited properties calculations for many materials.

2.2 Self-consistent field method

2.2.1 Hartree-Fock approximation

Besides the density functional theory, the solutions to the single-particle Schrödinger equation Eq. (2.1) can be derived by a self-consistent iterative approach. In the Hartree-Fock approximation, the trial wavefunction in the form of a single Slater determinant is used to be the ground state many-electron wavefunction [35]

$$\Psi_{HF}(r_1\sigma_1, \dots, r_N\sigma_N) = \begin{vmatrix} \phi_1(r_1\sigma_1) & \dots & \phi_1(r_N\sigma_N) \\ \vdots & \vdots & \vdots \\ \phi_N(r_1\sigma_1) & \cdots & \phi_N(r_N\sigma_N) \end{vmatrix}. \tag{2.5}$$

The variational principle requires the variation of the ground state energy with respect to the single-particle orbitals ϕ_i to be zero,

$$\frac{\delta\langle\Psi_{HF}|H|\Psi_{HF}\rangle}{\delta\phi_i} = 0. \tag{2.6}$$

Then the set of Hartree-Fock equations can be solve iteratively

$$-\frac{\hbar^2}{2m}\nabla^2\phi_i(r,\sigma) + V(r)\phi_i(r,\sigma) + V_H(r)\phi_i(r,\sigma) + \sum_{\sigma'}\int V_x(r,r',\sigma,\sigma')\phi_i(r',\sigma')dr'$$

$$= \varepsilon_i\phi_i(r,\sigma). \tag{2.7}$$

The exchange term $V_x(r,r',\sigma,\sigma') = -\sum_j \frac{e^2}{|r-r'|}\phi_j^*(r',\sigma')\phi_j(r,\sigma)$ represents the effective electron interactions from the Pauli exclusion principle, and stems from the antisymmetric form of the many-electron wavefunction. The quantitative solution to the Hartree-Fock equations is hard to get, but analytical solutions in the homogeneous interacting electron gas system can be derived rigorously.

2.2.2 Variational principles

The variational procedure used in deriving the Hartree-Fock equations dooms the interpretation of the eigenvalues cannot be the electron excitation energies. Nonetheless, according to the Koopman's theorem, the eigenvalues and eigenfunctions of the Hartree-Fock Hamiltonian can be regarded as the ground state energies of the many-electron system. This happens to me to coincide with the way of finding eigenvalues in the DFT framework, though we do not refer to the Koopman's theorem in DFT.

Personally, I am always enchanted by the beauty of the variational method used to solve the ground state of electron-electron interacting Hamiltonian in condensed matter physics. This further reminds me of the science fiction "*Story of Your Life*" by *Ted Chiang*. He embedded the variational principle in the field of optics in the fiction, to address the topic of free will and how people deal with the inevitable quoted from the fiction:

“The thing is, while the common formulation of physical laws is causal, a variational principle like Fermat’s is purposive, almost teleological.”

Figure 2.1 The Heptopod language in the movie *Arrival*, which is adapted from the fiction *Story of Your Life*. The language is graphic, and does not have start or end, which represents the notion of teleology. “Despite knowing the journey and where it leads, I embrace it. And I welcome every moment of it.”

Ted described the way human reckon on physics to be in a chronological and causal manner, where causes and effects grow from past to future as a chain reaction. In contrast, the physical intuition of heptapods, which are extraterrestrial creatures, are based on a teleological interpretation of events. They view events over a period of time, and find the requirements that have to be satisfied to reach a goal. This perspective requires the knowledge of initial and final states of the goal, or put it another way, the effects are needed before the causes are initiated.

This perhaps articulates what variational principles looks like to me. By the requirement of the variation of ground-state energy corresponds to an extremum, the Euler-Lagrange equations can be determined, so are the ground-state energies. I cannot help thinking about the theme of the fiction, “from the beginning I knew my destination, and I chose my route accordingly. But am I

working toward an extreme of joy, or of pain? Will I achieve a minimum, or a maximum?" I wish I could always stand on the positive side and persist to every dream that I have.

2.3 Quasiparticle excitations

2.3.1 Dyson equation

The DFT wavefunctions give a starting point for calculating the excited state properties. Generally, a perturbation scheme is used to calculate the changes in the quasiparticle excitations when screened Coulomb interactions are included. In the one-particle Green's function formalism, the excitations are treated by perturbing the exact ground state by quasiparticles or collective excitations with finite lifetimes [36]. The Feynman diagram for the irreducible self-energy Σ is shown in Figure 2.2. The sum over an infinite number of repeated graphs is given by the Dyson equation

$$iG = iG_0 + iG_0(-i\Sigma)iG. \tag{2.8}$$

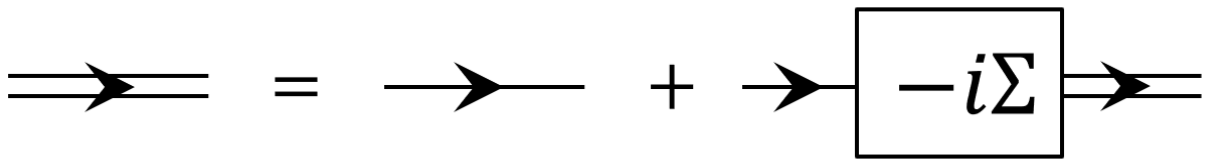

Figure 2.2 Green's function representation of the Dyson equation.

A general approximation of the self-energy is the GW approximation [26], where $\Sigma = iGW$ is a direct product of the Green's function G and the screened Coulomb interaction W in the first order. Explicitly, the Dyson equation in the GW scheme reads

$$\left(-\frac{\hbar^2}{2m}\nabla^2 + V_{ion}(r) + V_H(r)\right)\Phi_{nk}(r) + \int dr'\Sigma(r,r';E_{nk})\Phi_{nk}(r') = E_{nk}\Phi_{nk}(r), \quad (2.9)$$

the self-energy operator is

$$\Sigma(r,r';E) = i\int \frac{dE'}{2\pi}e^{-i\delta E'}G(r,r';E-E')W(r,r';E'). \quad (2.10)$$

The energy dependence on both sides of the Dyson equation indicates that an iterative self-consistent solution is needed. The Green's function can be obtained by single-particle eigenfunctions $\phi_{nk}(r)$ and eigenvalues ε_{nk} from DFT calculations

$$G(r,r';E) = \sum_{nk}\frac{\phi_{nk}(r)\phi_{nk}^*(r')}{E-\varepsilon_{nk}-i\delta_{nk}}, \quad (2.11)$$

and the screened Coulomb interaction in real space reads

$$W(r,r';E) = \sum_{qGG'}e^{i(q+G)\cdot r}W_{GG'}(q,E)e^{-i(q+G')\cdot r'}. \quad (2.12)$$

In the reciprocal space, the screened Coulomb interaction is a product of the inverse dielectric function and the bare Coulomb interaction

$$W_{GG'}(q,\omega) = \epsilon_{GG'}^{-1}(q,\omega)v(q+G'). \quad (2.13)$$

Taking only the diagonal term from the self-energy operator, the Dyson equation Eq. (2.9) can then be expressed as

$$E_{nk} = \varepsilon_{nk} - \langle nk|V_{xc}|nk\rangle + \langle nk|\Sigma(E_{nk})|nk\rangle, \tag{2.14}$$

where the exchange-correlation energy from the DFT is replaced by the self-energy operator that includes many-body interactions to estimate the quasiparticle energy E_{nk}. The Eq. (2.14) needs to be solved iteratively.

In practice, the solution to Eq. (2.9) is obtained by a first-order perturbation to the DFT ground-state energy

$$E_{nk} = E_{nk}^{0} + \frac{d\sum_{nk}(\varepsilon_{nk})/dE}{1 - d\sum_{nk}(\varepsilon_{nk})/dE}(E_{nk}^{0} - \varepsilon_{nk}), \tag{2.15}$$

where

$$E_{nk}^{0} = \varepsilon_{nk} - \langle nk|V_{xc}|nk\rangle + \langle nk|\Sigma(\varepsilon_{nk})|nk\rangle. \tag{2.16}$$

Then the quasiparticle energies based on a single-particle excitation can be obtained from a meanfield calculation of the electron wavefunction and energies.

2.3.2 Dielectric function and random phase approximation

One key component in understanding the many-body interactions in condensed matter systems is the dielectric response function. It dictates the response of a material to external fields, such as electromagnetic and optical probes. It is also one of the building blocks in the determination of the screened Coulomb interaction $W = \epsilon^{-1}v$, and thus, the excited quasiparticle properties.

In the linear response theory, the dielectric function for a periodic system is usually expressed as a matrix in the reciprocal lattice vectors [30],

$$\delta V(q+G,\omega) = \sum_{G'} \epsilon^{-1}_{GG'}(q,\omega)\delta V_{ext}(q+G',\omega). \quad (2.17)$$

The off-diagonal elements in the dielectric matrix $\epsilon_{GG'}(q,\omega)$ reflect the charge inhomogeneity of the crystal, where a long-wavelength external perturbation can render short-wavelength fields in a crystal. This effect is also known as the local-field effect.

There are some well-known forms of the dielectric function in certain limits. In the long-wavelength limit, the dielectric function for a three-dimensional homogeneous electron gas can be simplified to

$$\epsilon(q \to 0,\omega) = 1 - \frac{\omega_p^2}{\omega^2}, \quad (2.18)$$

where $\omega_p = \sqrt{\frac{4\pi n e^2}{m}}$ is the classical plasma frequency. In the static limit with $q \ll k_F$, the famous Thomas-Fermi screening function is obtained

$$\epsilon(q,\omega=0) = 1 + \frac{K_s^2}{q^2}, \quad (2.19)$$

where $K_s^2 = 4\pi e^2 D(\varepsilon_F)$, and $D(\varepsilon_F)$ is the density of states at the Fermi energy ε_F.

The polarizability χ relates the external perturbation δV_{ext} to the change in the electron density $\delta\rho$ in an interacting electron system $\delta\rho = \chi\delta V_{ext}$. Similarly, the independent-particle polarizability describes the response to the total perturbing potential $\delta\rho = \chi_0\delta V$. Ignoring the exchange-correlation potential, $\delta V = \delta V_{ext} + \delta V_H = \delta V_{ext} + V_c\delta\rho$, where V_c is the bare Coulomb interaction. Recall that the dielectric response function relates δV_{ext} and δV by $\delta V = \epsilon^{-1}\delta V_{ext}$. Combining the results together, one arrives at the random phase approximation (RPA)

$$\epsilon_{RPA} = 1 - V_c\chi_0. \tag{2.20}$$

Within the formalism of DFT, the RPA polarizability is given by

$$\chi^0_{GG'}(q,\omega) = \frac{1}{\Omega}\sum_{nn'k}(f_{nk} - f_{n'k+q})\frac{M^*_{nn'}(k,q,G)M_{nn'}(k,q,G')}{\varepsilon_{nk} - \varepsilon_{n'k+q} + \hbar\omega + i\hbar 0^+}, \tag{2.21}$$

where $M_{nn'}(k,q,G) = \langle nk+q|e^{iG\cdot r}|n'k\rangle$. Intuitively, the RPA polarizability takes into account all possible transitions from occupied to unoccupied states that contribute to screening. The contribution is dictated by the transition amplitude and the transition energy between the initial and final states. RPA is generally used in the GW approximation to calculate the screened Coulomb interaction.

2.3.3 Generalized plasmon-pole model

The frequency dependence in the dielectric function $\epsilon^{-1}_{GG'}(q,\omega)$ makes it the bottleneck in excited state properties calculations. In practice, only the static polarizability is calculated within the generalized plasmon-pole (GPP) model [26]. The calculation of the self-energy is usually broken into two parts, the screened exchange operator Σ_{SX} and the Coulomb-hole operator Σ_{CH}, $\Sigma = \Sigma_{SX} + \Sigma_{CH}$,

$$\langle nk|\Sigma_{SX}(E)|n'k\rangle = -\sum_{n''}\sum_{qGG'}M^*_{n''n}(k,-q,-G)M_{n''n'}(k,-q,-G')$$

$$\times \epsilon^{-1}_{GG'}\big(q, E - \varepsilon_{n''k-q}\big)v(q+G'), \tag{2.22}$$

$$\langle nk|\Sigma_{CH}(E)|n'k\rangle = \frac{i}{2\pi}\sum_{n''}\sum_{qGG'}M^*_{n''n}(k,-q,-G)M_{n''n'}(k,-q,-G')$$

$$\times \left[\epsilon^{-1}_{GG'}\right]^h \left(q, E - \varepsilon_{n''k-q}\right) v(q+G'), \tag{2.23}$$

where

$$\left[\epsilon^{-1}_{GG'}\right]^h (q,E) = \frac{1}{\pi} P \int_0^\infty dE' \frac{\mathrm{Im}\epsilon^{-1}_{GG'}(E')}{E-E'}. \tag{2.24}$$

In the GPP model, the full frequency dependence is included in the inverse dielectric function by a single-pole

$$\mathrm{Re}\epsilon^{-1}_{GG'}(q,\omega) = \delta_{GG'} + \frac{\Omega^2_{GG'}(q)}{\omega^2 - \omega^2_{GG'}(q)}, \tag{2.25}$$

where $\Omega_{GG'}(q)$ is the plasmon-pole strength and $\omega_{GG'}(q)$ is the plasmon-pole frequency. Finally, under GPP model, Eq. (2.24) can be written as

$$\left[\epsilon^{-1}_{GG'}\right]^h (q,\omega) = \frac{1}{2} \frac{\Omega^2_{GG'}(q)}{\omega_{GG'}(q)(\omega - \omega_{GG'}(q))}. \tag{2.26}$$

2.4 Optical properties and excitonic effects

2.4.1 Bethe-Salpeter equation

The screening dielectric function discussed previously is the longitudinal dielectric function to external electromagnetic probes. It is in principle a density-density response function. In order to study the optical properties of a many-electron interacting system, the appropriate dielectric function to describe the response from transverse electromagnetic probes is the transverse dielectric function, which is a current-current response function.

Optical properties, on the other hand, depends highly on the excitonic effects of the system. Excitons are formed when an electron is kicked out to the conduction band, and a hole is left in the valence band. The Coulomb interaction between the electron and hole dictates the binding energy of excitons. Exciton states generally are a coherent superposition of interband transitions, and needs to be described by a two-particle excitation picture. Bethe-Salpeter equation (BSE) [27] encodes the electron-hole interaction in the interaction kernel K^{eh}, which is composed of a direct K^d and an exchange term K^x. K^d represents the e-h attractive interactions, and K^x describes the repulsive exchange energy,

$$\langle vck|K^d|v'c'k'\rangle = \sum_{GG'} M_{cc'}(k,q,G) W_{GG'}(q;0) M^*_{vv'}(k,q,G'), \tag{2.27}$$

$$\langle vck|K^x|v'c'k'\rangle = \sum_{GG'} M_{cv}(k,q,G) v(q+G) \delta_{GG'} M^*_{c'v'}(k,q,G'). \tag{2.28}$$

K^x dictates the exciton triplet and singlet splitting, and is determined by the wavefunction overlap between the valence and conduction states. K^d can be decomposed into three parts

$$\langle vck|K^d|v'c'k'\rangle = \frac{a_{vck,v'c'k'}}{q^2} + \frac{b_{vck,v'c'k'}}{q} + c_{vck,v'c'k'}, \tag{2.29}$$

where

$$a_{vck,v'c'k'} = M_{cc'}(k,q,0) \epsilon^{-1}_{00}(q) M^*_{vv'}(k,q,0), \tag{2.30}$$

$$b_{vck,v'c'k'} = \sum_G \left\{ M_{cc'}(k,q,G) \frac{\epsilon^{-1}_{G0}(q)}{|q+G|} M^*_{vv'}(k,q,0) + M_{cc'}(k,q,0) \frac{\epsilon^{-1}_{0G}(q)}{|q+G|} M^*_{vv'}(k,q,G) \right\}, \tag{2.31}$$

$$c_{vck,v'c'k'} = \sum_{G\neq 0}\sum_{G'\neq 0} M_{cc'}(k,q,G)\frac{\epsilon^{-1}_{GG'}(q)}{|q+G||q+G'|}M^{*}_{vv'}(k,q,G'), \tag{2.32}$$

are called the "head", "wing", and "body", respectively.

Based on the e-h interaction kernel K^{eh}, the BSE is then like the Schrödinger equation, with the single-particle Hamiltonian replaced by the two-particle kernel

$$\left(E^{QP}_{ck} - E^{QP}_{vk}\right)A^{S}_{vck} + \sum_{v'c'k'}\langle vck|K^{eh}|v'c'k'\rangle = \Omega^{S}A^{S}_{vck}, \tag{2.33}$$

where A^{S}_{vck} is the exciton wavefunction, and Ω^{S} is the exciton excitation energy. According to the Tamm-Dancoff approximation, an exciton state is represented by including only the linear superpositions of valence to conduction interband transitions

$$|S\rangle = \sum_{vck} A^{S}_{vck}|vck\rangle. \tag{2.34}$$

And the real-space exciton wavefunction can be expressed as

$$\Psi(r_e, r_h) = \sum_{vck} A^{S}_{vck}\psi_{k,c}(r_e)\psi^{*}_{k,v}(r_h). \tag{2.35}$$

In practice, the exciton wavefunction is plotted in real-space by fixing the position of the hole.

2.4.2 Optical absorption spectra

The optical absorption spectra are obtained from Fermi golden rule. Without the *e-h* interaction, it is a direct summation of the oscillator strength from independent vertical transitions

$$\epsilon^{0}_{2}(\omega) = \frac{16\pi^2 e^2}{\omega^2}\sum_{vck}|e\cdot\langle vk|\hat{v}|ck\rangle|^2\delta(\omega - E^{QP}_{ck} + E^{QP}_{vk}), \tag{2.36}$$

where $\hat{v}$ is the velocity operator along the polarization direction of light. It is worth pointing out that from the formula, a large joint density of states (JDOS) in the electronic band structure will lead to large oscillator strengths of the vertical transitions [30]. With the e-h interaction, the optical spectra will be largely modified by the coherent superposition of e-h pairs

$$\epsilon_2(\omega) = \frac{16\pi^2 e^2}{\omega^2} \sum_S |e \cdot \langle 0|\hat{v}|S\rangle|^2 \delta(\omega - \Omega^S). \tag{2.37}$$

For 2D systems, it is more convenient to renormalize the dielectric function into the optical absorbance $A(\omega)$ in order to make direct comparison with experiments

$$A(\omega) = \frac{\omega \epsilon_2(\omega) d}{c}, \tag{2.38}$$

where d is the periodic distance perpendicular to the 2D material plane, and c is the speed of light. $A(\omega)$ describes the fraction of incident photon that is absorbed by the 2D material.

Overall, the excitonic effect is strong in reduced dimension materials and materials with large JDOS. The reduced dielectric screening in low-dimensions makes the effective e-h Coulomb interaction stronger, resulting in large exciton binding energies. On the other hand, large JDOS helps facilitate the coherent superposition of e-h pairs, hence enhancing the optical transition oscillator strength.

Chapter 3: Phonon Assisted Optical Transitions in Transition Metal Dichalcogenides

3.1 Introduction

Exciton is the quasiparticle formed by an electron excited to the conduction band and the left hole in the valence band, which are bounded by the Coulomb interaction. However, not all excitons are optically bright. For spin orbit splitting bands, according to the exciton selection rules, only the excitons with electrons and holes residing in the same spin configuration bands can be accessed by light, and hence are called bright excitons. Besides, since photons have negligible momentum, the excitons with Coulomb bound electrons and holes at different high symmetry points in the Brillouin zone are also optically dark. The momentum dark excitons can be activated via coupling with phonons, which can provide the needed momentum transfer [30,37].

MoS_2 is a typical transition metal dichalcogenide, which exhibits indirect band gap in few layer and bulk form, but becomes a direct band gap material in the monolayer limit [11]. Because of the direct band gap and reduced dielectric screening in monolayer MoS_2, the exciton effects dominate its optical properties and result in drastically enhanced photoluminescence compared with bulk MoS_2. In this chapter, we will present the work on first principles calculations of the exciton states in MoS_2 as well as MoS_2/WS_2 heterostructure, and the effect of lattice vibrations (phonon) on the exciton states.

3.2 Computational methods

Density functional theory (DFT) is a widely used first principles method to calculate the ground state electronic properties of materials. Center to the theory is the Kohn-Sham equation [24]

$$\left(-\frac{1}{2}\nabla^2 + V_{ion} + V_H + V_{xc}^{DFT}\right)\psi_{nk}^{DFT} = E_{nk}^{DFT}\psi_{nk}^{DFT}, \tag{3.1}$$

which is obtained by variational method on a fictitious non-interacting system. Therefore, DFT can only capture the ground state properties of materials. However, excitons consist of excited electrons in the conduction band, which are excited state properties. Besides, DFT always underestimates the band gap. If we want to study exciton effects in first principles calculations, we must go beyond DFT.

Using DFT as a starting point, GW approximation [26] treats the quasiparticle self-energy $\sum(E_{nk}^{QP})$ as the first term of the expansion in terms of the single particle Green's function G and the screened Coulomb interaction W. The one particle excitation energies are then solved by the Dyson equation

$$\left(-\frac{1}{2}\nabla^2 + V_{ion} + V_H + \sum(E_{nk}^{QP})\right)\psi_{nk}^{QP} = E_{nk}^{QP}\psi_{nk}^{QP}, \tag{3.2}$$

GW approximation can give very accurate band gaps. The correlated electron-hole (exciton) excited state wavefunction and excitation energy can be further solved by the Bethe-Salpeter equation (BSE) [27]

$$\left(E_{ck}^{QP} - E_{vk}^{QP}\right)A_{vck}^{S} + \sum_{v'c'k'}\langle vck|K^{eh}|v'c'k'\rangle = \Omega^{S}A_{vck}^{S}. \tag{3.3}$$

where K^{eh} is the electron-hole interaction kernel. The exciton states are a collective state formed by different electron-hole pairs at different k points in the Brillouin zone modulated by the exciton wavefunction A^S_{vck}

$$|S\rangle = \sum_{vck} A^S_{vck} |vck\rangle. \quad (3.4)$$

Based on these theories, we can study the exciton effects in materials with first principles calculations. The DFT calculations are performed with the package Quantum ESPRESSO [38,39]. And for the GW+BSE calculations, the package BerkeleyGW [40] is used.

3.3 Monolayer MoS_2

The interlayer interaction for bulk MoS_2 is Van der Waals interaction, hence it is easy to exfoliate few layer MoS_2 from the bulk. The atomic structure for monolayer MoS_2 is shown in Figure 3.1. The Mo atom is sandwiched by two layers of S atoms. Unlike the indirect band gap with valence band maximum (VBM) at Γ and conduction band minimum (CBM) at K in few layer MoS_2, monolayer MoS_2 has direct band gap at K valley. The band structure at DFT level (note that DFT band structure gives the wrong indirect band gap) is shown in Figure 3.2 (a), and the GW band gap correction is shown in Table 3.1. Since the indirect band gap $\Gamma_v \rightarrow K_c$ is comparable to the direct band gap $K_v \rightarrow K_c$, besides the bright exciton state at K valley, we also expect there to be momentum dark excitons formed by the transitions $\Gamma \rightarrow K$. However, in the package BerkeleyGW, only the direct transitions in momentum space are considered. In order to study the indirect transitions, a supercell with lattice constant $\sqrt{3}$ times the unit cell is used to

fold the band at K back to Γ point, so that the transitions from Γ_v to K_c can also be captured by the calculation. The band structure calculated with the supercell is shown in Figure 3.2 (b).

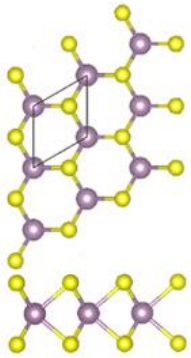

Figure 3.1 Atomic structure of monlayer MoS_2: top view (upper panel) and side view (lower panel). The parallelogram represents the unit cell.

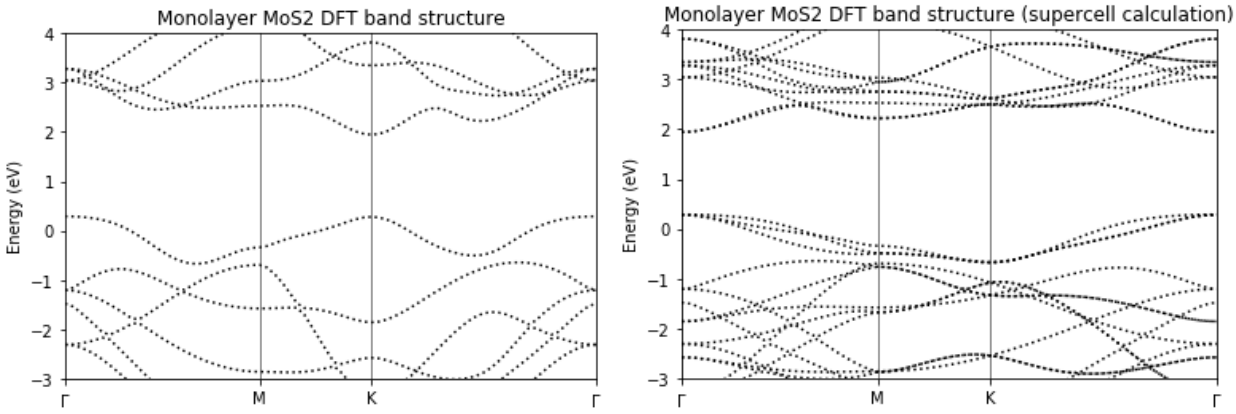

Figure 3.2 Monolayer MoS_2 band structure at DFT level in (a) unit cell calculation (b) supercell calculation.

Table 3.1 DFT/GW band gap and exciton energy for monolayer MoS_2

Energy unit: eV	DFT gap $(K \to K)$	DFT gap $(\Gamma \to K)$	GW gap $(K \to K)$	GW gap $(\Gamma \to K)$	1st bright exciton energy	Exciton binding energy
Monolayer	1.666	1.657	2.586	2.718	1.903	-0.683

Besides, we would like to consider the effect of lattice vibrations on the exciton states. Using second order harmonic approximation, the equation of motion for the atoms is [30]

$$M_j \ddot{\xi}_j^{\alpha} = -\sum_{j'\alpha'} A_{jj'}^{\alpha\alpha'} \xi_{j'}^{\alpha'}. \tag{3.5}$$

We are interested in the normal modes of the atomic vibrations (the collective motion of the atoms forms the quasiparticle, phonon), where each atom with mass M_j moves periodically with the same frequency ω

$$\xi_j^{\alpha}(t) = C_j^{\alpha} \frac{1}{\sqrt{M_j}} e^{-i\omega t}. \tag{3.6}$$

By plugging this into the equation of motion, we get the dynamical matrix $D_{jj'}^{\alpha\alpha'}(\boldsymbol{q})$ for the lattice vibrations

$$\omega^2 C_j^{\alpha} = \sum_{j'\alpha'} D_{jj'}^{\alpha\alpha'}(\boldsymbol{q})\, C_{j'}^{\alpha'}. \tag{3.7}$$

We can get the dynamical matrix with first principles calculations, and the eigenvectors of the matrix describe the motion of the atom j in the direction α. By shifting the atomic positions according to the different phonon modes, we can use first principles calculations to simulate the effects of lattice vibrations.

For the momentum dark exciton $\Gamma_v \rightarrow K_c$, according to momentum conservation of optical transitions, the phonon at K point (hence with momentum $\boldsymbol{q} = \boldsymbol{K}$) can compensate the momentum required to fulfill the transition. The calculated phonon dispersion along the path Γ to K in the first Brillouin zone [Figure 3.3 (b)] is shown in Figure 3.3 (a). Here I mainly focus on the low energy acoustic phonon modes, as in low energy settings only the acoustic phonons can

be excited and are populated. The atomic motions for the TA1, TA2 and LA phonon modes are depicted in Figure 3.4. For the TA1 mode, Mo atoms move in the out of plane direction and S atoms move in the in-plane direction; for the TA2 mode, Mo atoms move in the in-plane direction and S atoms move in the out of plane direction; for the LA mode, both Mo and S atoms move in the in plane direction. Since for 2D materials, in the out of plane direction atoms feel less interatomic interactions, intuitively we would expect the LA phonon mode to have the strongest effect on the exciton states.

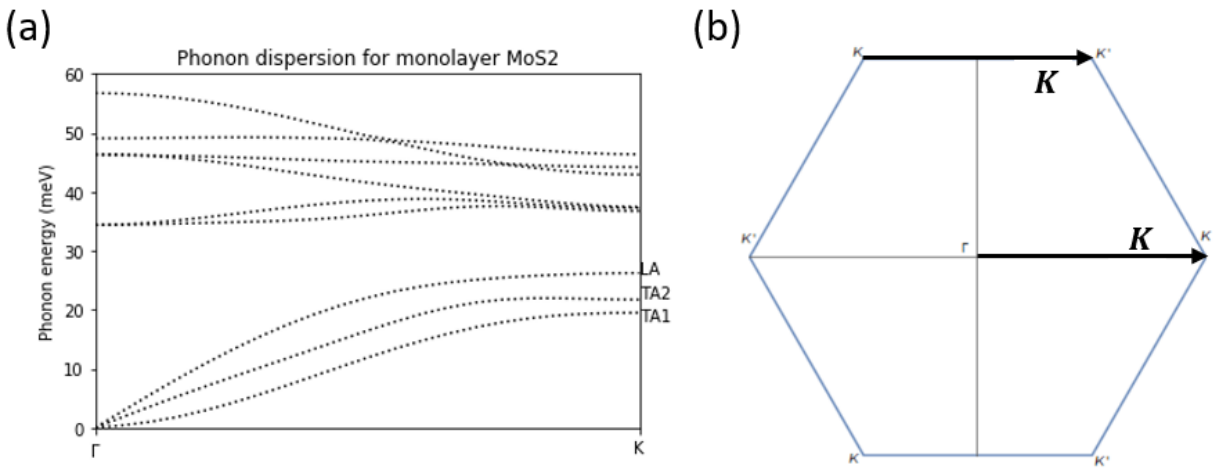

Figure 3.3 (a) Phonon dispersion for monolayer MoS_2. (b) First Brillouin zone of hexagonal lattice. The transitions with momentum $\boldsymbol{K}$ are labeled by black arrows.

The calculated exciton states for monolayer MoS_2 are shown in Table 3.2. For the unit cell calculations, the first two excitons are from the direct $K \rightarrow K$ and $K' \rightarrow K'$ transitions (in the first Brillouin zone there are two K points). The higher energy exciton states are the higher energy level states (2p, 2s, etc.) of the direct excitons. The first bright exciton energy is 1.903 eV, agrees well with the experimental value of 1.90 eV. The high binding energy makes the exciton observable at room temperature.

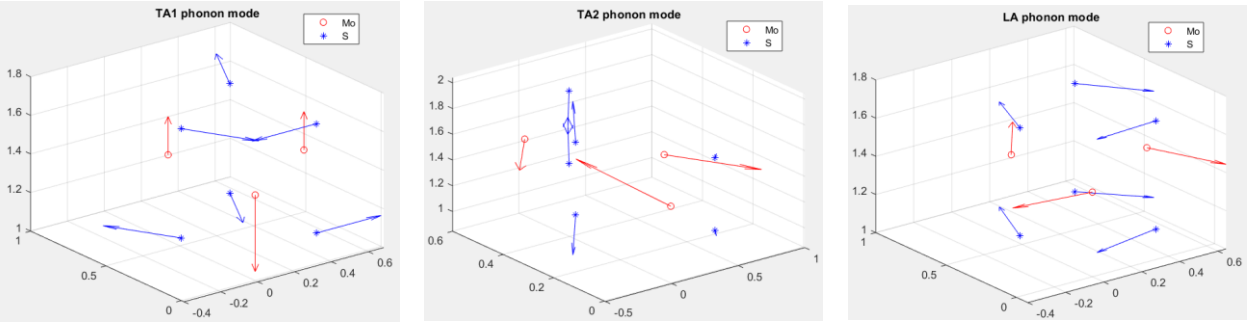

Figure 3.4 Schematic diagrams of the atomic vibrations for the TA1 phonon mode (left panel), TA2 phonon mode (middle panel) and LA phonon mode (right panel).

Table 3.2 Exciton states for monolayer MoS_2 with unit cell and supercell calculations (quantities in the bracket represent the transition dipole oscillator strength)

Monolayer MoS2 (unit: eV)	1st exciton energy	2nd exciton energy	3rd exciton energy	4th exciton energy	5th exciton energy	6th exciton energy
Unit cell	1.903 (3×10^3) $(K_v\ to\ K_c)$	1.904 (3×10^3) $(K_v'\ to\ K_C')$	2.107 (2×10^{-1})	2.120 (2×10^{-2})	2.136 (2×10^{1})	2.138 (1×10^{1})
$\sqrt{3}$ cell original structure	1.901 (4×10^3) $(K_v\ to\ K_c)$	1.901 (1×10^3) $(K_v'\ to\ K_C')$	1.903 (6×10^{-2}) $(K_v\ to\ K_C')$	1.903 (5×10^{-2}) $(K_v'\ to\ K_c)$	2.040 (1×10^{-5}) $(\Gamma\ to\ K_c)$	2.040 (2×10^{-5}) $(\Gamma\ to\ K_C')$
$\sqrt{3}$ cell LA phonon shifted structure	1.898 (3×10^3) $(K_v\ to\ K_c)$	1.898 (5×10^2) $(K_v'\ to\ K_C')$	1.903 (5×10^2) $(K_v\ to\ K_C')$	1.903 (3×10^2) $(K_v'\ to\ K_c)$	2.046 (1×10^3) $(\Gamma\ to\ K_c)$	2.046 (2×10^2) $(\Gamma\ to\ K_C')$

For the supercell calculation, besides the bright direct excitons, we observe four dark excitons, which originate from the indirect $K_v \rightarrow K_c'$, $K_v' \rightarrow K_c$, $\Gamma_v \rightarrow K_c$ and $\Gamma_v \rightarrow K_c'$ transitions. Based on

the calculated exciton energies and GW band gap, we can calculate the binding energies of the direct and indirect excitons, as shown in Table 3.3. We see that the indirect excitons have similar binding energies with that of the direct excitons.

Table 3.3 Direct/Indirect exciton binding energies for monolayer and bilayer MoS_2

Exciton binding energy (eV)	Unit cell direct exciton ($K \rightarrow K$)	$\sqrt{3}$ cell direct exciton ($K \rightarrow K$)	$\sqrt{3}$ cell Indirect exciton ($\Gamma \rightarrow K$)
Monolayer	-0.683	-0.691	-0.678
bilayer	-0.520	-0.501	-0.501

Then for the supercell calculation with the shifted atomic positions according to LA phonon mode, we do observe that the indirect excitons $\Gamma_v \rightarrow K_c$ and $\Gamma_v \rightarrow K_c'$ now have the same order of oscillator strength with the direct excitons, confirming that the LA phonon mode can brighten the indirect exciton by momentum transfer. Besides, the excitons $K_v \rightarrow K_c'$ and $K_v' \rightarrow K_c$ also pick up large oscillator strength under the effect of LA phonon mode. In fact, the $K \rightarrow K'$ momentum change is the same as $\Gamma \rightarrow K$, as shown in Figure 3.3 (b), hence the phonon with momentum $\boldsymbol{K}$ can not only render the $\Gamma \rightarrow K$ exciton bright, but also the $K \rightarrow K'$ excitons.

3.4 Bilayer MoS_2

There are different stacking styles for MoS_2, as shown in Figure 3.5. Here we adopt the AA' stacking, which is the more common stacking style observed in experiments. Bilayer MoS_2 has indirect band gap with the VBM at Γ and CBM at K. The DFT band structure for bilayer MoS_2 is shown in Figure 3.6.

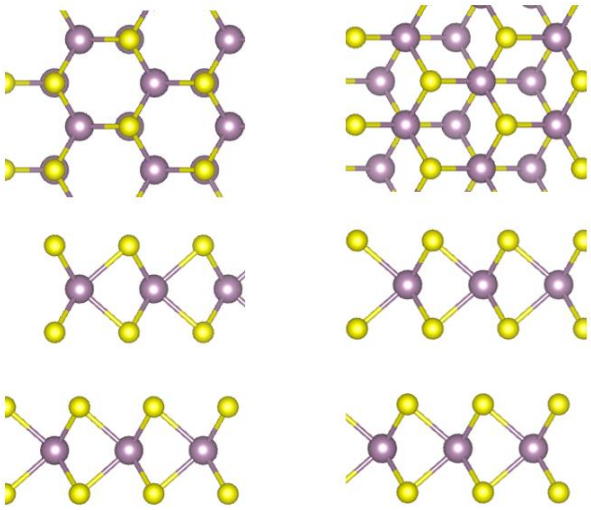

Figure 3.5 AA' stacking (left panel) and AB stacking (right panel) for bilayer MoS_2

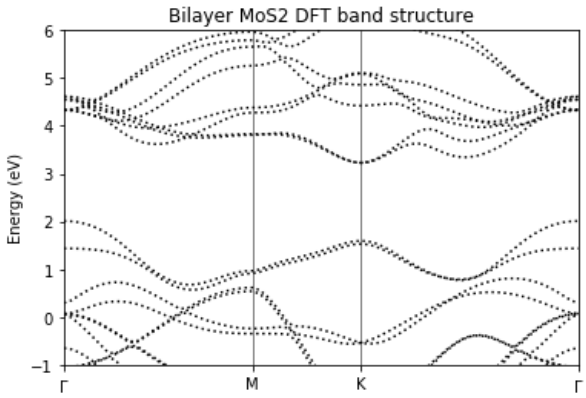

Figure 3.6 Band structure for AA' stacking bilayer MoS_2 at DFT level

For bilayer, since the dielectric screening is increased, we would expect smaller exciton binding energies. The exciton state calculations are shown in Table 3.3, and are consistent with our expectations. Then in order to study the indirect excitons and phonon effects, I again introduced the supercell calculations and atomic position shifts. The corresponding results are shown in Table 3.3 and Table 3.4, respectively. Again, we see that the indirect excitons have similar

binding energies as the direct excitons, and that the LA phonon mode has most significant effect on the exciton oscillator strength.

Table 3.4 Exciton states for bilayer MoS_2

$\sqrt{3}$ cell Bilayer calculation (eV)	1st dark exciton ($\Gamma \rightarrow K$) energy (oscillator strength)	1st bright exciton ($K \rightarrow K$) energy (oscillator strength)
Original structure	1.611 (1×10^{-5})	1.901 (4×10^{2})
TA1 phonon	1.613 (1×10^{-6})	1.889 (1×10^{3})
TA2 phonon	1.613 (3×10^{-5})	1.891 (1×10^{3})
LA phonon	1.613 (3×10^{-2})	1.880 (1×10^{3})

3.5 MoS_2/WS_2 heterostructure

For heterostructures, there are typically two band alignments, as shown in Figure 3.7. For type I band alignment, the VBM and CBM are in the same layer, hence the lowest energy exciton state is an intralayer exciton. For type II band alignment, the VBM and CBM are in different layers, and the lowest energy exciton is an interlayer exciton which typically has longer life time than intralayer exciton. The DFT band structure for the MoS_2/WS_2 heterostructure is shown in Figure 3.8.

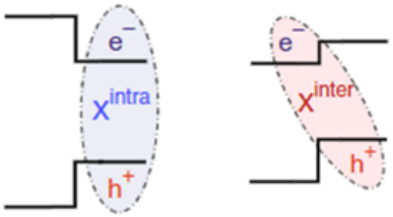

Figure 3.7 Type I band alignment with intralayer exciton (left panel) and type II band alignment with interlayer exciton (right panel) in heterostructure

The calculated exciton states using supercell for the MoS2/WS2 heterostructure are shown in Table 3.5.

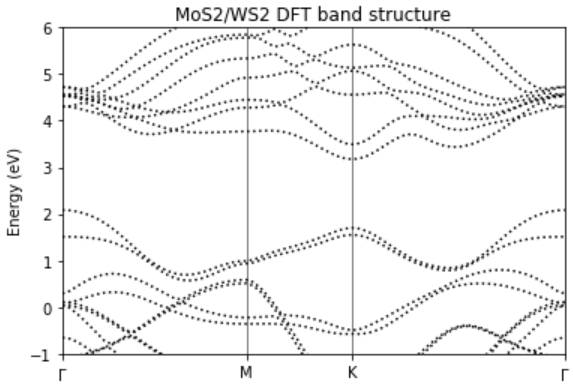

Figure 3.8 MoS_2/WS_2heterostructure band structure at DFT level

Table 3.5 Exciton states in MoS_2/WS_2heterostructure

1st dark exciton (unit: eV)	DFT band gap ($\Gamma_{v1} \rightarrow K_{c1}$)	GW band gap ($\Gamma_{v1} \rightarrow K_{c1}$)	1st dark exciton energy	Exciton binding energy
$\sqrt{3}$ cell	1.10	1.98	1.47	-0.51

1st bright exciton (2-degenerate)	DFT band gap ($K_{v1} \rightarrow K_{c1}$)	GW band gap ($K_{v1} \rightarrow K_{c1}$)	1st bright exciton energy	Exciton binding energy
$\sqrt{3}$ cell	1.47	2.25	1.78	-0.47

2nd bright exciton (2- degenerate)	DFT band gap ($K_{v2} \rightarrow K_{c1}$)	GW band gap ($K_{v2} \rightarrow K_{c1}$)	2nd bright exciton energy	Exciton binding energy
$\sqrt{3}$ cell	1.62	2.39	1.84	-0.55

In order to study the phonon effect and band to band optical transitions of the heterostructure, I calculated the non-electron-hole interaction (without exciton) optical transitions under the atomic position shifts. This can serve as a good estimate for the exciton states. For the phonon modes,

now that the two layers are different, there are two different LA phonon modes. LA1 consists only MoS_2 layer motions and both W and S atoms move in-plane, while LA2 mode consists only MoS_2 layer motions and both Mo and S atoms move in-plane. The phonon effect on the non-eh transition oscillator strength is shown in Table 3.6. An interesting phenomenon with the phonon effect is that the LA1 phonon has stronger effect on the $\Gamma_{v1} \rightarrow K_{c2}$ transition, while the LA2 phonon has stronger effect on the $\Gamma_{v1} \rightarrow K_{c1}$ transition. Along with the physical motion of the phonon modes, we infer that the CBM (K_{c1}) consists of Mo atom orbitals while the second lowest conduction band (K_{c2}) mainly consists of W atom orbital. To check this inference, I calculated the partial density of states for the MoS_2/WS_2 heterostructure, as shown in Figure 3.9. The PDOS at K (right panel) confirms our expectation, and clearly shows the type II band alignment at K point.

Table 3.6 Non-electron-hole interaction optical transition oscillator strength for MoS_2/WS_2

Non-eh transition to K_{c1}	$\Gamma_{v1} \rightarrow K_{c1}$	$K_{v1} \rightarrow K_{c1}$	$K_{v2} \rightarrow K_{c1}$
Original structure	4×10^{-12}	0.68	9.42
LA1 phonon mode shifted structure	1×10^{-5}	0.68	9.41
LA2 phonon mode shifted structure	2×10^{-3}	0.68	9.35

Non-eh transition to K_{c2}	$\Gamma_{v1} \rightarrow K_{c2}$	$K_{v1} \rightarrow K_{c2}$	$K_{v2} \rightarrow K_{c2}$
Original structure	8×10^{-12}	10.58	0.56
LA1 phonon mode shifted structure	7×10^{-3}	10.57	0.56
LA2 phonon mode shifted structure	2×10^{-6}	10.57	0.56

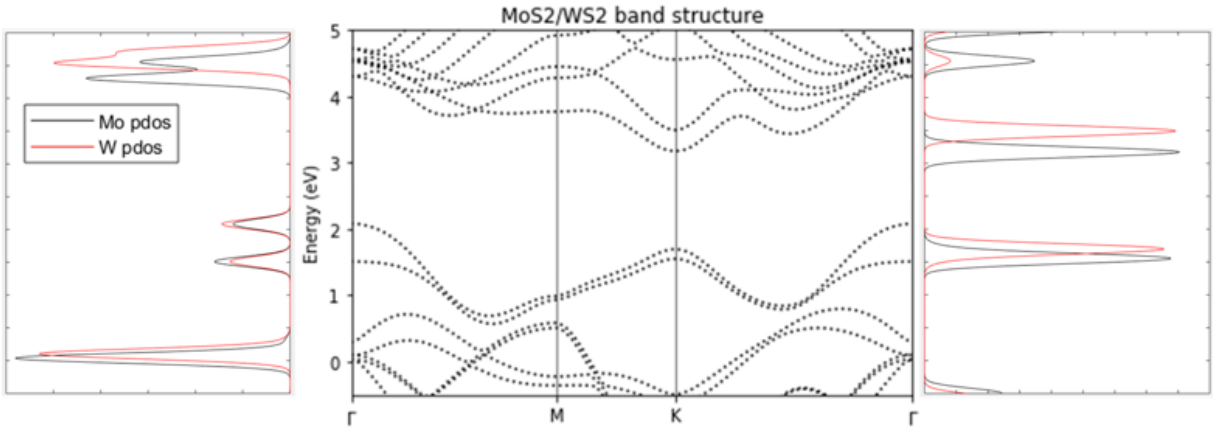

Figure 3.9 Partial density of state at Γ point (left panel) and K point (right panel)

3.6 Conclusions

In conclusion, we have studied the direct and indirect exciton states for monolayer MoS_2, bilayer MoS_2 and MoS_2/WS_2 heterostructure by first principles calculations, with the application of a supercell to fold the band at K to Γ. We found that the indirect $\Gamma_v \rightarrow K_c$ exciton has similar binding energy as the direct $K_v \rightarrow K_c$ exciton, implying its significance under interactions with phonon, which can apply the momentum required to fulfill the indirect optical transition. The phonon effect is investigated with atomic position shifts according to the phonon modes, and we found that the LA phonon mode has the most significant effect on the indirect exciton state.

Chapter 4: Quasiparticle and Optical Properties of Correlated Magnet $CrCl_3$

4.1 Introduction

Layered van der Waals (vdW) magnetic materials have attracted significant research interest to date. In this chapter, we employ the first-principles many-body perturbation theory to calculate excited-state properties of a prototype vdW magnet, chromium trichloride ($CrCl_3$), covering monolayer, bilayer, and bulk structures. Unlike usual nonmagnetic vdW semiconductors, in which many-electron interactions and excited states are sensitive to dimensionality, many-electron interactions are always enhanced and dominate quasiparticle energies and optical responses of both two-dimensional and bulk $CrCl_3$. The electron-hole (*e-h*) binding energy can reach 3 eV in monolayer and remains as high as 2 eV in bulk. Because of the cancellation effect between self-energy corrections and *e-h* binding energies, the lowest-energy exciton ("optical gap") is almost not affected by the change of dimensionality. In addition, for the excitons with similar *e-h* binding energies, their dipole oscillator strength can differ by a few orders of magnitude. Our analysis shows that such a big difference is from a unique interference effect between complex exciton wave functions and interband transitions. Finally, we find that the interlayer stacking sequence and magnetic coupling barely change quasiparticle band gaps and optical absorption spectra of $CrCl_3$. Our calculated low-energy exciton peak positions agree with available measurements. These findings give insight into the understanding of many-electron interactions and the interplay between magnetic orders and optical excitations in vdW magnetic materials.

Many-electron interactions are known to be enhanced in low-dimensional structures, and they dominate corresponding excited-state properties. Because of the reduced screening, electronic self-energy and excitonic effects are dramatically enhanced. For instance, the electron-hole (*e*-*h*) binding energy of monolayer transition metal dichalcogenides [11,25,41–45] and black phosphorus [8–11] can be around a few hundred meV, which is about one to two orders of magnitude larger than those of typical bulk semiconductors [11,45,47–51]. This reduced screening effect stems from the surrounded vacuum and, thus, is sensitive to dimensionality. For example, *e*-*h* binding energy of bulk Tellurium is less than 10 meV, while that of its monolayer structure is increased to be around 700 meV [52]. In addition to screening, the electronic band dispersion (effective mass) also impacts many-electron interactions. Particularly, flat bands contribute to a large joint density of states (JDOS), enhancing the chance of forming *e*-*h* pairs [15]. However, there have been very limited studies to clarify the roles of dimensionality and band-curvature effects on many-electron interactions and excitonic effects to date.

Recently achieved two-dimensional (2D) magnetic materials [16–19] may provide a unique opportunity to answer this fundamental question because their electronic band edges are usually dominated by localized 3*d* orbitals and are flat for both 2D and bulk structures. With the help of magnetic anisotropy [20], these 2D structures hold a long-range magnetic order by gapping low-energy modes of magnons [21]. Because of enhanced light-matter interactions, layered van der Waals (vdW) magnetic structures exhibit significant magneto-optical effects, such as the magneto-optical Faraday and Kerr effects, and magnetic circular dichroism (MCD), which have been applied to identify magnetic orders [55,56,60] and give rise to optomagnetic applications based on vdW structures [61,62]. More recently, enhanced excitonic effects on magneto-optical responses have been calculated for monolayer magnetic structures [63,64]. These theoretical

works showed that *e-h* binding energy can be 1.7 eV in monolayer CrI_3 [63], which is substantially larger than those of other nonmagnetic semiconductors and satisfactorily explained available measurements.

Chromium trichloride ($CrCl_3$) is a good candidate to explore the relationship between many-electron interactions and dimensionality in correlated vdW magnetic structures. Unlike the widely studied CrI_3, whose bulk exhibits a ferromagnetic (FM) order [18,27], bulk $CrCl_3$ exhibits an interlayer antiferromagnetic (AFM) order with an intralayer FM order [19], the so-called A-type AFM order. Moreover, because of the significantly smaller spin-orbit coupling (SOC), the magnetic anisotropy energy is small in $CrCl_3$ [57,59], and its 2D structure may exhibit an in-plane ground state magnetism [19,28,29] and rich topological spin textures, such as meron-like pairs at finite temperatures [30]. This weak SOC also substantially simplifies the optical spin selection rules, making $CrCl_3$ ideal to analyze many-electron interactions and corresponding optical activities.

In this chapter, we have employed first-principles many-body perturbation theory (MBPT) to study many-electron interactions and excited-state properties of $CrCl_3$. Significant self-energy corrections and excitonic effects are discovered for monolayer, bilayer, and bulk $CrCl_3$. Our calculated exciton energies are in good agreement with available measurements for both monolayer and bulk structures. Interestingly, for excitons with similar *e-h* binding energies within the same structure, their dipole oscillator strength can be different for a few orders of magnitude. Our analysis shows that this big difference is from a unique interference effect between the complex exciton wave functions and interband transition matrices. Moreover, we show that many-electron interactions and excitonic effects are less sensitive to dimensionality in these vdW magnets. Thus, the flat bands and enhanced JDOS play an important role in deciding

excited-state properties, giving hope to robust room-temperature excitons in bulk magnets. Finally, we find that these optical spectra and many-electron effects have little dependence on the interlayer crystallographic structure or magnetic orders. Therefore, magneto-optical effects [56,60] or second-harmonic generation [69,70] may be applied to identify those complex symmetries of ultra thin magnets.

4.2 Atomic structures and computational details

The atomic structures of $CrCl_3$ are presented in Figure 4.1. Below 240 K [19], bulk $CrCl_3$ is a vdW layered material adopting the rhombohedral phase (space group $R\bar{3}$), which is formed by an interlayer shift along the $(\vec{a} - \vec{b})$ direction, as shown in Figures 4.1 (a1) and 4.1 (a2). This is also known as the low-temperature (LT) phase. Above 240 K, it experiences a crystallographic phase transition into the monoclinic phase (space group *C2/m*), which is formed by an interlayer shift along the $-\vec{a}$ direction, as shown in Figures 4.1 (b1) and 4.1 (b2). This is the high-temperature (HT) phase. Such a structural phase transition is similar to that observed in bulk CrI_3 [27]. Within each single layer of $CrCl_3$, the chromium atoms are arranged in a honeycomb structure, and each chromium atom is surrounded by six chloride atoms forming an octahedra. Below 17 K, an intralayer FM order is formed in bulk $CrCl_3$, followed by an interlayer AFM order below 14 K [19]. The magnetic moments are dominantly hosted on chromium atoms. The interlayer AFM/FM orders are schematically shown in the Figures 4.1 (a2) and 4.1 (b2), respectively, with each layer taking the FM order within the layer.

The ground-state properties are obtained by density functional theory (DFT) within the general gradient approximation using the Perdew-Burke-Ernzerhof exchange-correlation functional [33]

as implemented in the Quantum ESPRESSO package. The vdW interactions in bilayer and bulk $CrCl_3$ are included via the semiempirical Grimme-D3 scheme [34]. Semicore 3*p* and 3*d* electrons of chromium atoms are included in norm-conserving pseudopotentials [73], and the plane-wave energy cutoff is set to be 65 Ry. A vacuum distance of 18 Å between adjacent layers is used along the periodic direction in monolayer and bilayer calculations to avoid spurious interactions. SOC is relatively small in $CrCl_3$ due to the small atomic number of the ligand atom and, hence, is not considered in our calculations. Figure 4.2 (a) and (b) show the band structure of monolayer $CrCl_3$ with and without SOC effect, respectively. From both the band structure and the partial density of states (PDOS), we can see that the SOC has little effect on $CrCl_3$ since SOC strength varies as the fourth power of the atomic number, and both elements in $CrCl_3$ have relatively small atomic numbers [57,59]. Therefore, in our calculations we do not consider the SOC effect.

The MBPT calculations are performed using the BerkeleyGW code [37] including the slab Coulomb truncation for monolayer and bilayer structures. Quasiparticle (QP) energy is calculated by using the single-shot G_0W_0 approximation within the general plasmon pole model [38]. The Bethe-Salpeter equation (BSE) is employed to obtain excitonic effects and optical absorption spectra [39]. Because of the depolarization effect [40,41], only the incident light polarized parallel to the atomic plane (the in-plane direction) is considered for the monolayer and bilayer cases. Ten valence bands and six conduction bands are included in optical calculation to provide converged spectra below 3.5 eV. For monolayer and bilayer $CrCl_3$, a coarse *k* grid of 9x9x1 is adopted to calculate the dielectric function and QP energies, and it is interpolated to a fine *k* grid of 18x18x1 for the *e-h* interaction kernel and solving BSE. The coarse *k* grid is set to be 9x9x2 and the fine *k* gird is set to be 18x18x4 for bulk $CrCl_3$. The convergence test shows that the error bar of this *k*-point sampling is within 0.1 eV for *GW* band gaps and exciton energies.

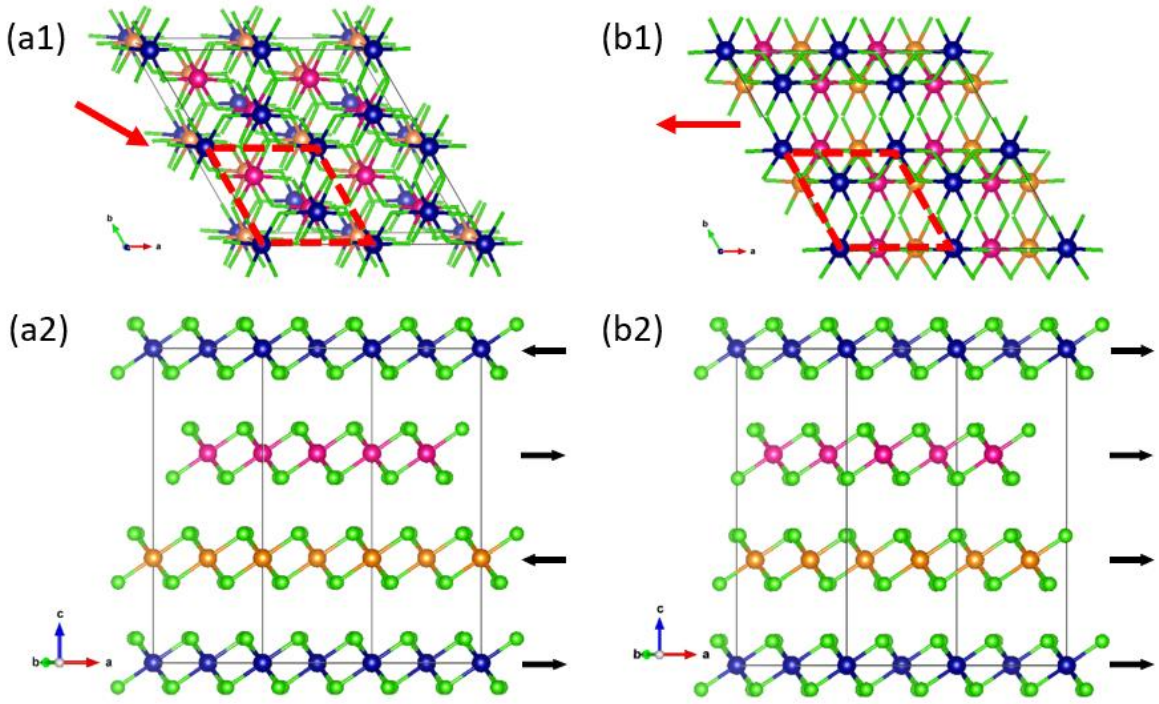

Figure 4.1 (a1) and (a2) Top and side views of the rhombohedral (LT) structure. (b1) and (b2) top and side views of the monoclinic (HT) structure. Cr atoms in different layers are shown with different colors. The Cl atoms are not shown in top views [(a1) and (b1)) for clarity. The arrows in (a1) and (b1) show the relative interlayer shift direction. The structure in (a1) is slightly shifted along the interlayer shift direction for clarity. The unit cells are marked by red dashed lines. The interlayer AFM/FM orders are schematically shown in (a2) and (b2), respectively, by the black arrows representing atomic spin directions in each FM ordered layer. The polarizations are shown in the in-plane direction to reflect the experimentally observed in-plane magnetic polarizations, although only collinear polarizations are considered in the calculations.

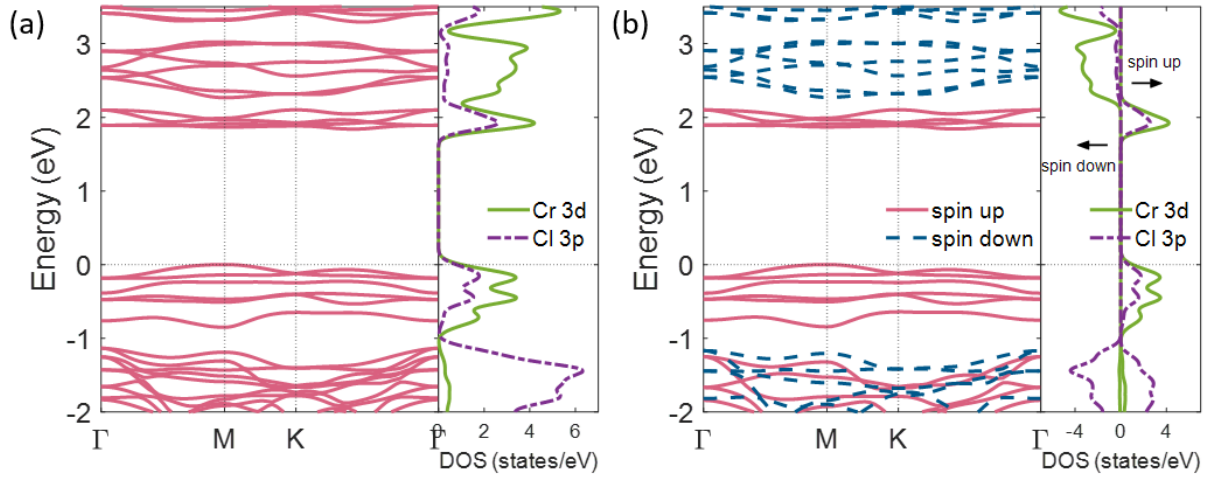

Figure 4.2 DFT level band structure and partial density of states of monolayer $CrCl_3$ with intralayer FM order (a) with SOC effect and (b) without SOC effect. The energy of the valence band maximum is set to be zero.

We have also tested the convergence of band gap and exciton energy on coarse *k* grid for monolayer $CrCl_3$. When the *k* grid goes from 9x9x1 to 18x18x1, the quasiparticle band gap change is within 50 meV and the X_1, X_2 exciton energy change is within 100 meV. Therefore, we use the coarse *k*-gird of 9x9x1 for monolayer and bilayer calculations, and 9x9x2 for bulk calculations.

Table 4.1 Convergence test of DFT and *GW* band gaps, X_1 and X_2 exciton energies on coarse *k*-grid for monolayer $CrCl_3$. The unit is eV.

Coarse *k*-grid	DFT band gap	*GW* band gap	X_1 exciton energy	X_2 exciton energy
9x9x1	1.84	4.66	1.48	2.25
12x12x1	1.84	4.64	1.52	2.28
18x18x1	1.84	4.63	1.56	2.32

4.3 Monolayer $CrCl_3$

The DFT-calculated band structure of an FM monolayer $CrCl_3$ is presented in Figure 4.3 (a). For FM monolayer $CrCl_3$, the valence band maximum (VBM) is located at the high-symmetry M point and the conduction band minimum (CBM) is located around the middle point of the $K - \Gamma$ line, resulting in an indirect band gap of 1.84 eV and a direct band gap of 1.87 eV at M point. According to the projected density of states (PDOS) in Figure 4.3 (a), the four lowest-energy conduction bands and the five highest-energy valence bands have a sizable amount of 3p orbital components of chloride atoms. Interestingly, those higher-energy (spin down) conduction bands between 2.5 and 3.5 eV are nearly from pure 3d orbitals of chromium atoms. Finally, both the valence and conduction band edges exhibit relatively flat dispersions and are composed of the same spin (up) states. This enhanced JDOS indicates strong many-electron interactions and potentially active interband transitions due to the spin-allowed selection rule [15].

We have calculated QP energies within the *GW* approximation. The DFT and *GW* band gaps are summarized in Table 4.2. The indirect QP band gap is 4.66 eV, and the direct QP band gap is 4.69 eV. The linear fit of *GW*-calculated quasiparticle energies to DFT eigenvalues is presented in Figure 4.3 (b). Due to the reduced dielectric screening of the suspended 2D structure and enhanced JDOS, QP energy corrections in monolayer $CrCl_3$ are significant, rendering a 2.82 eV enlargement of the *GW* band gap from the DFT result. This enhancement is larger than those in monolayer MoS_2 (~ 1.0 eV) [4,6] and black phosphorus (~ 1.2 eV) [10], indicating that correlated flat bands further enhance many-electron interactions in addition to the dimensionality factor.

We have further calculated the optical absorption spectrum of FM monolayer $CrCl_3$. To avoid the artificial effect from the choice of vacuum space in simulations, we plot the optical absorbance by $A(\omega) = \frac{\omega d}{c}\varepsilon_2(\omega)$, where $\varepsilon_2(\omega)$ is the calculated imaginary part of the dielectric function and d represents the distance between adjacent $CrCl_3$ layers along the periodic direction of our calculation. Figure 4.4 (a) shows the optical absorbance of monolayer $CrCl_3$ with and without excitonic effects included. In the absence of *e-h* interactions, the absorbance (blue dashed line) edge starts at around 4.7 eV, corresponding to the QP direct band gap at the *M* point. This significant absorption edge is consistent with the enhanced JDOS and allowed spin-selection rule as shown in Figure 4.3 (a).

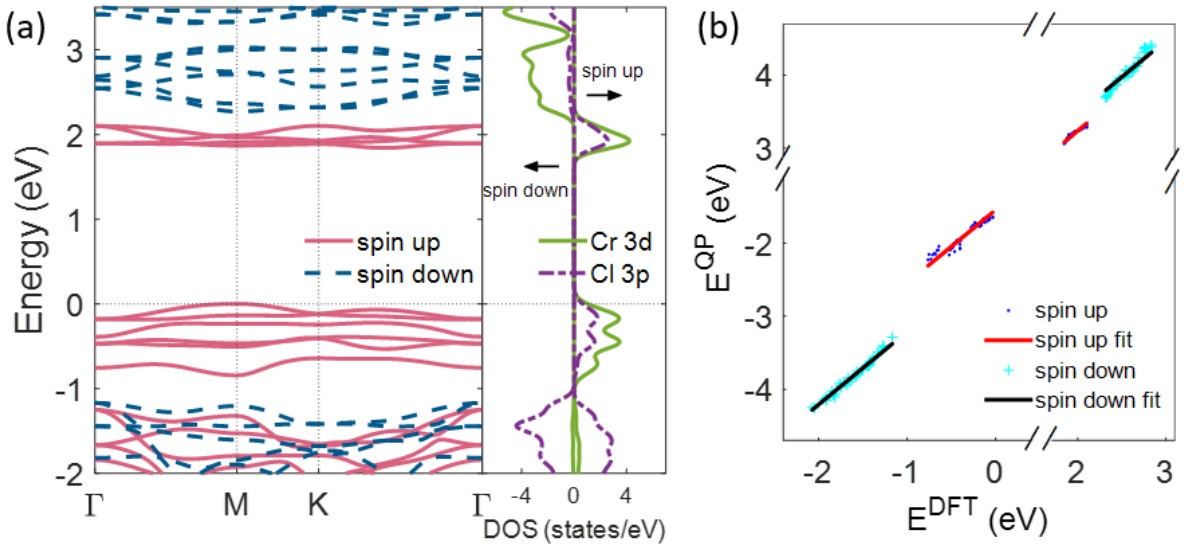

Figure 4.3 (a) DFT-calculated band structure (left panel) and projected density of states (right panel) of monolayer $CrCl_3$ with an intralayer FM order. The energy of the valence band maximum is set to be zero. (b) Linear fit of QP energies to DFT eigenvalues for monolayer $CrCl_3$.

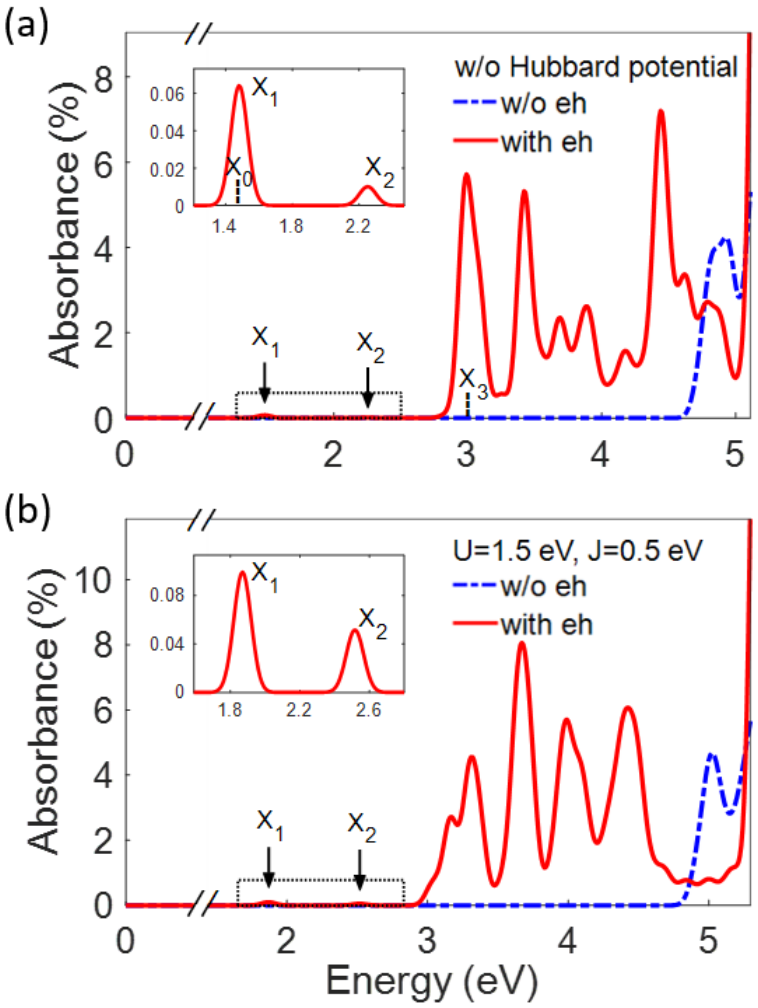

Figure 4.4 Absorbance of monolayer $CrCl_3$ without *e-h* interaction (blue dashed line) and with *e-h* interaction (red solid line) calculated on top of (a) DFT ground state and (b) DFT+U ground state (with Hubbard parameters U = 1.5 eV, J = 0.5 eV). The two characteristic absorption peaks are marked as X_1 and X_2, respectively. A dark exciton state below X_1 is marked as X_0 in the inset of (a). An exciton state at higher energy is marked as X_3 in (a).

After *e-h* interactions are included, the optical absorption spectrum is dramatically changed. The main optical absorption happens between 3 and 5 eV, which is a 2-eV red shift from the

interband-transition result. Importantly, we observe two characteristic excitonic peaks in the optical spectrum at the low energy regime, which are marked as X_1 and X_2 at 1.48 and 2.25 eV in Figure 4.4 (a), respectively. It is worth mentioning that more excitonic states are around X_1 and X_2 while most of them are optically dark. In the inset of Figure 4.4 (a), we also mark the lowest-energy dark exciton, X_0, whose energy is about 20 meV below X_1 but its dipole oscillator strength is about four orders of magnitude smaller than that of X_1. These low-energy excitons result in significant exciton binding energies of 3.23, 3.21, and 2.44 eV for X_0, X_1, and X_2, respectively. Such exciton binding energies are enormous compared with those of other typical 2D semiconductors such as monolayer MoS_2 (~ 960 meV) [4] and black phosphorous (~ 800 meV) [10], and they are almost two times larger than that of the sibling magnetic material, monolayer CrI_3 (~ 1.7 eV) [25]. The *e-h* binding energy of the lowest bright X_1 exciton is even larger than the self-energy (*GW*) correction. As a result, the "optical gap" (1.48 eV) is lower than the DFT band gap (1.84 eV). Recent photoluminescence measurements of monolayer and multilayer $CrCl_3$ at 2 K found a single peak around 1.43 eV [66]. This agrees with our MBPT results, where the X_1 exciton is located at 1.48 eV.

We have tested the dependence of MBPT results on top of the DFT ground state with Hubbard potential, denoted by DFT+U/MBPT. We choose the Hubbard parameters [43] U = 1.5 eV and J = 0.5 eV as an example [26]. The band structure and PDOS for monolayer $CrCl_3$ at this DFT+U level are presented in the Figure 4.5. To avoid the double-counting problem in this DFT+U/MBPT scheme, we have subtracted the DFT+U-level Hubbard potential V_{Hub} together with the DFT exchange-correlation potential V_{xc} from the conventional self-energy operator $\Sigma(E)$ within the *GW* approximation, following Ref. [25,44,45] by

$$[T + V_{ext} + V_H + V_{xc} + V_{Hub}]\Psi(\boldsymbol{r}) + \int d\boldsymbol{r}' \Delta\Sigma(\boldsymbol{r}, \boldsymbol{r}'; E^{qp})\Psi(\boldsymbol{r}') = E^{qp}\Psi(\boldsymbol{r}), \quad (4.1)$$

and

$$\Delta\Sigma(E) = \Sigma(E) - V_{xc} - V_{Hub}. \quad (4.2)$$

The DFT+U/MBPT absorption spectra of monolayer $CrCl_3$ are shown in Figure 4.4 (b). After Hubbard potential is included, the DFT+U level band gap is around 150 meV larger than the DFT band gap, and the *GW* quasiparticle indirect gap is increased by about 180 meV to 4.84 eV, as seen from the onset of the absorbance without *e-h* interaction in Figure 4.4 (b). The optical absorption spectrum from DFT+U ground state also shows a significant blue shift. For example, the X_1 exciton energy is increased by around 400 meV to 1.87 eV. Given the better correspondence with available measurements [66] in the absence of the Hubbard potential, we use the DFT/MBPT scheme without U in the following calculations of bilayer and bulk $CrCl_3$.

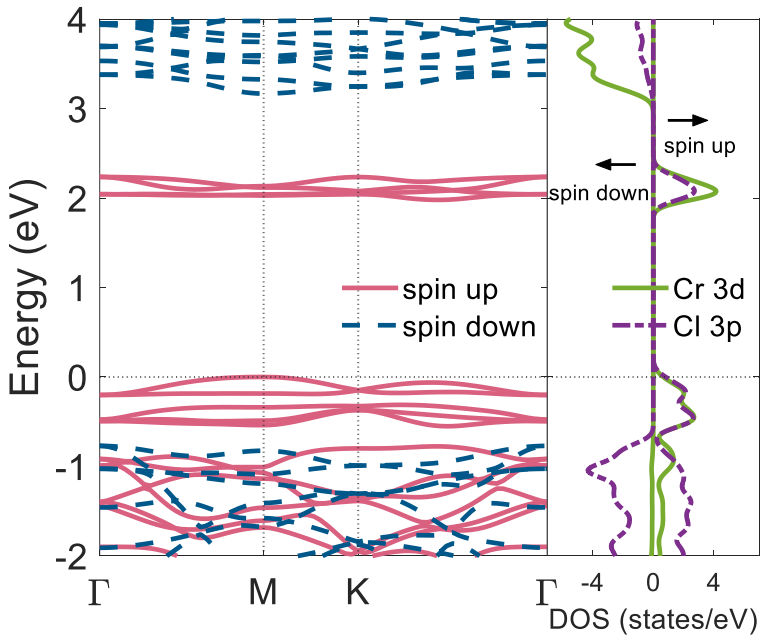

Figure 4.5 DFT+U level band structure (left panel) and DOS (right panel) for monolayer $CrCl_3$ with Hubbard parameters U = 1.5 eV, J = 0.5 eV.

Moving to higher excitation energies (between and 5 eV), there are exciton states with much stronger dipole oscillator strength than those lower-energy exciton states. For example, the peak marked by X_3 in Figure 4.4 (a) has an oscillator strength two orders larger than that of X_1. These bright excitons dominate the main optical absorption spectrum.

To better understand these strongly bound excitons, we have plotted the real-space exciton wave functions of X_0, X_1 and X_3 with the hole positioned on a chromium atom in Figures 4.6 (a) - (c). Because of the large *e-h* binding energy, all three excitons exhibit highly localized wave functions. Particularly, for X_0 and X_1, their wave functions are nearly confined within one unit cell. These highly localized real-space wave functions indicate a smearing of the *e-h* pair contributions from the whole Brillouin zone (BZ) in reciprocal space. This also agrees with the argument that those flat bands around band edges actively contribute to the formation of strongly bound excitons. For X_3, because of its smaller *e-h* binding energy, the wave function is slightly broader and roughly covers the size of three unit cells.

It is hard to tell any significant difference from the real-space wave functions of excitons X_0 and X_1, whose dipole oscillator strength differ, however, by four orders of magnitude. Following Ref. [46], we try to find the original contributions of dipole oscillator strength of these excitons. We rewrite the optical transition matrix element $\langle 0|\hat{v}|i\rangle$ from the ground (vacuum) state $|0\rangle$ to an exciton state $|i\rangle = \sum_{vck} A^i_{vck}|vc\rangle$ (A^i_{vck} is the exciton amplitude solved from the BSE [39]), to analyze the contribution of interband transition matrix elements $\langle vk|\hat{v}|ck\rangle$ at a certain energy ω to the optical transition matrix element

$$\langle 0|\hat{v}|i\rangle = \sum_{vck} A^i_{vck}\langle vk|\hat{v}|ck\rangle = \int S_i(\omega)\, d\omega, \tag{4.3}$$

where

$$S_i(\omega) = \sum_{vck} A^i_{vck} \langle vk|\hat{v}|ck\rangle \delta(\omega - (E_{ck} - E_{vk})), \tag{4.4}$$

and

$$I_i(\omega) = \int_0^{\omega} S_i(\omega')d\omega'. \tag{4.5}$$

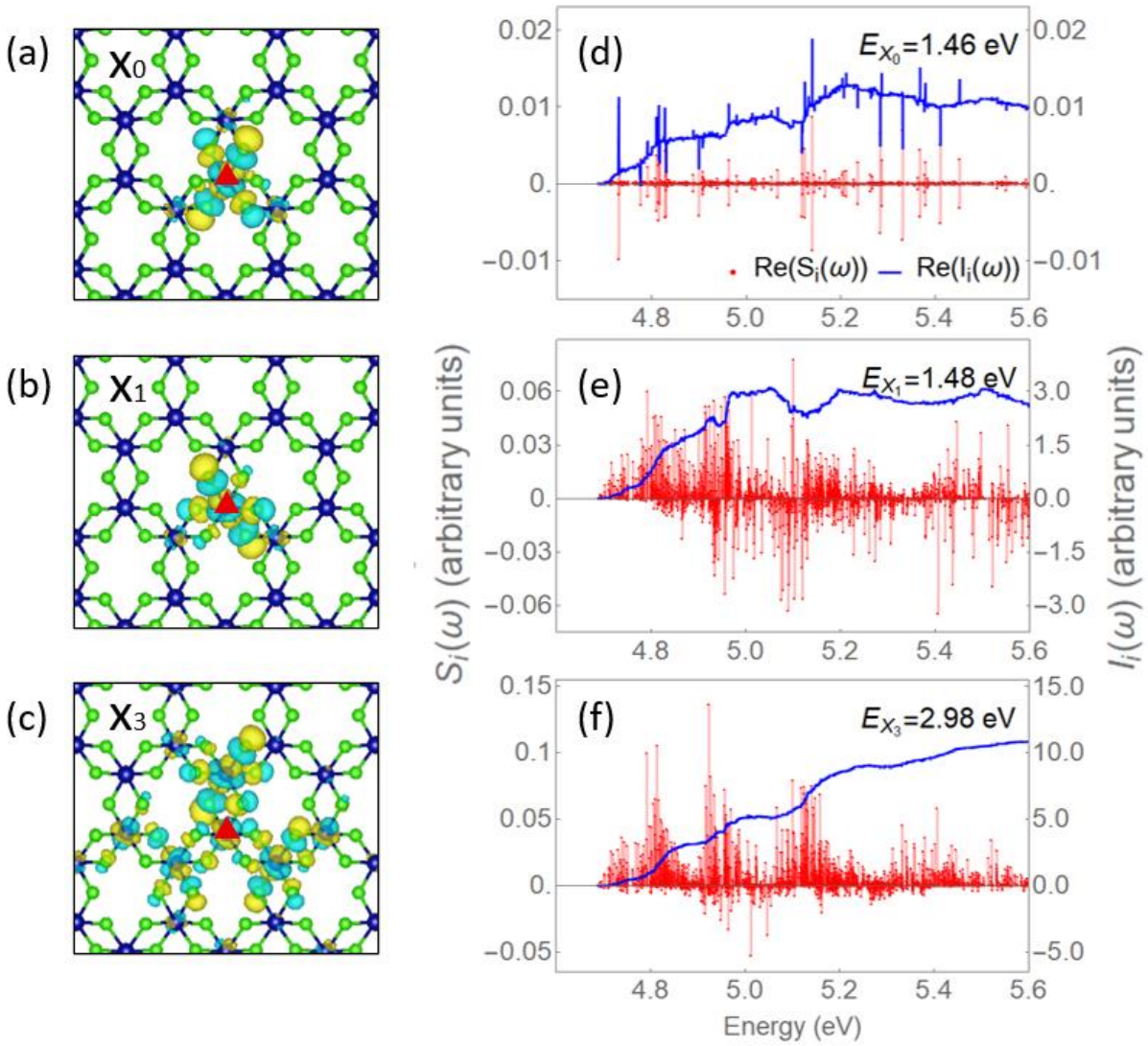

Figure 4.6 (a)-(c) Real-space wave functions of exciton states X_0, X_1 and X_3 in monolayer $CrCl_3$, respectively. The hole positions are marked with red triangles. (d)-(f) $S_i(\omega)$ and its integral $I_i(\omega)$ for exciton states X_0, X_1, and X_3, respectively.

The corresponding interference effect between the complex interband transition matrices ($\langle vk|\hat{v}|ck\rangle$) and exciton amplitude (A^i_{vck}) is essential for determining the overall dipole oscillator strength of excitons [note that the exciton dipole oscillator strength is proportional to the square of $I_i(\omega)$). Since monolayer $CrCl_3$ is FM and lacks time reversal symmetry, $S_i(\omega)$ and its integral $I_i(\omega)$ are complex functions. To address main characters, we only plot the real part of $S_i(\omega)$ and $I_i(\omega)$ in Figures 4.6 (d) - (f) for the exciton states X_0, X_1 and X_3, respectively. The imaginary part is similar. These plots essentially show how *e-h* interactions obtain dipole oscillator strength from interband transitions at different energies and reform them into corresponding excitons. Like previous studies on graphene [79], the energy distribution of $S_i(\omega)$ of all studied excitonic states is spread over a wide energy range, which is consistent with their large binding energies.

For the dark exciton X_0, there is a coherent cancellation of $S_i(\omega)$. As shown in Figure 4.6 (d), $S_i(\omega)$ fluctuates positively and negatively with similar amplitude at all energies. As a result, the integral of $S_i(\omega)$ is not able to build up over the energy range and produces a small overall $I_i(\omega)$. This is the reason for the tiny dipole oscillator strength of X_0. This interference effect between interband transition matrix elements and exciton wave functions is less prominent for the bight exciton state X_1, especially at the low energy side. As shown in Figure 4.6 (e), $I_i(\omega)$ grows dominantly from the quasiparticle band gap around 4.7 eV, and nearly saturates after 5 eV. This indicates that the dipole oscillator strength of the bright exciton X_1 is mainly

contributed by those flat bands around band edges. Finally, for the bright exciton X_3 in Figure 4.6 (f), there is only minor interference effect. Particularly, the interband contributions have nearly the same positive sign over the whole energy range. As a result, the integral $I_i(\omega)$ builds consistently along the way to higher transition energies, resulting in a large oscillator strength. In a word, the dramatically different optical dipole oscillator strength of excitons with similar *e-h* binding energy is mainly from the interference effect between the complex interband transitions and exciton amplitude involved in forming excitons.

4.4 Bilayer $CrCl_3$

Compared with monolayer $CrCl_3$, the interlayer magnetic order and stacking sequence in bilayer $CrCl_3$ bring more degrees of freedom. First, as shown in Figure 4.1, there are two crystallographic structures of bulk $CrCl_3$. Unlike bulk $CrCl_3$, recent experiments have shown that no crystallographic transition was observed in few layer $CrCl_3$, keeping a monoclinic HT phase structure at low temperatures [80]. Nevertheless, in order to identify the possible influence of crystallographic structure on the electronic and optical properties of bilayer $CrCl_3$, we consider both stacking sequences in our calculations. Second, the energy difference of interlayer FM and AFM orders is small, less than 5 meV/Cr as shown in previous calculations [57,81] and depends critically on the approach used [81]. Although interlayer AFM order is widely observed in available measurements [57,66,67,80], the FM order can be easily achieved by applying a small magnetic field as shown by recent experiments [57,66,67]. Therefore, we will consider both interlayer AFM and FM orders in the following calculations of bilayer $CrCl_3$.

The DFT-calculated band structures are summarized in Figure 4.7 for AFM/FM and LT/HT configurations of bilayer $CrCl_3$. For the interlayer AFM order shown in Figures 4.7 (a) and 4.7 (c), the bands of the two layers are almost degenerate, with opposite spin components from each layer. For the interlayer FM order shown in Figures 4.7 (b) and 4.7 (d), the two layers have the same spin components, resulting in an overall double-degenerated spin up band-edge states. Meanwhile, the

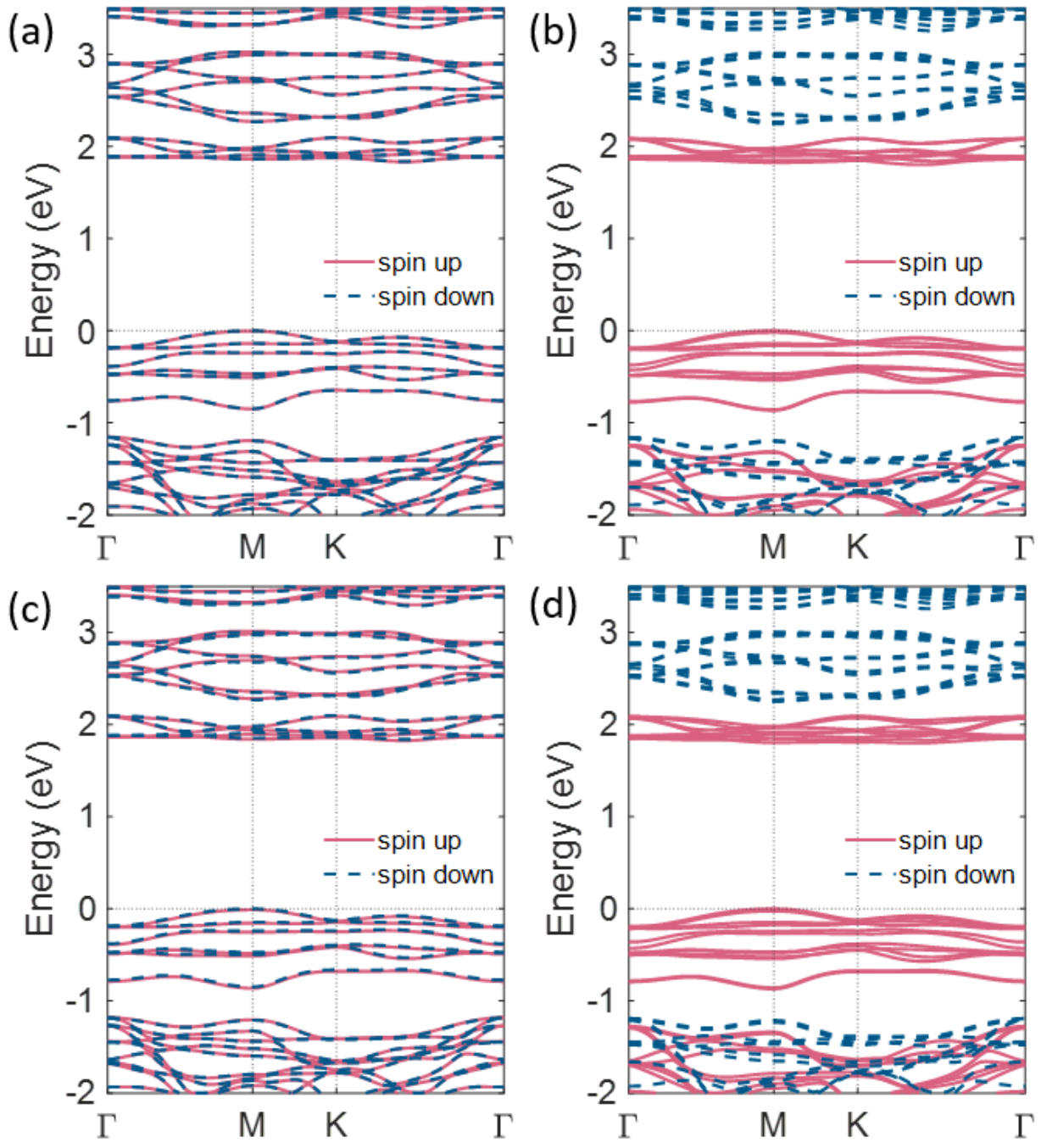

Figure 4.7 DFT-calculated band structure of bilayer $CrCl_3$: (a) LT rhombohedral stacking with an AFM interlayer coupling; (b) LT rhombohedral stacking with a FM interlayer coupling; (c) HT monoclinic stacking with an AFM interlayer coupling; (d) HT monoclinic stacking with a FM interlayer coupling. The energy of the valence band maximum is set to be zero.

band structures and band gaps of LT and HT phases are similar, except that the monoclinic HT structure exhibits a little larger splitting of the bands than the rhombohedral LT structure.

The *GW*-calculated QP energy vs the DFT results are summarized in Table 4.2. Because of the similar reasons for enhanced self-energy corrections as in monolayer $CrCl_3$, significant QP energy corrections are obtained in bilayer $CrCl_3$. For example, the QP band gap of bilayer rhombohedral LT phase AFM $CrCl_3$ is increased from a DFT value of 1.84 to 4.45 eV. As shown in Table 4.2, these self-energy corrections are not sensitive to the interlayer structure or magnetic order; the self-energy corrections are around 2.6 eV for all four configurations. On the other hand, this *GW* correction is around 200 meV smaller than that of monolayer. This is mainly from the increased screening in bilayer structures.

The optical absorption spectra of these four configurations are presented in Figure 4.8. Like the results of QP energies, the optical absorption spectra are similar for all four configurations. Therefore, many-electron effects and linear optical absorption spectra are not sensitive to the interlayer crystallographic structure and magnetic orders. Take the bilayer LT phase of AFM $CrCl_3$ as an example [Figure 4.8 (a)]. Without *e-h* interactions, the absorption edge starts at around 4.5 eV, which is due to the QP band gap. After including *e-h* interactions, a significant red shift of the optical spectrum is observed. Like the result of a monolayer, the main optical spectrum is still located between 3 and 5 eV, although the QP band gap is reduced by around 200 meV compared with monolayer. Moreover, the two characteristic excitonic peaks, X_1 and X_2, are observed in all spectra. Their energies are similar for all four configurations as well. Interestingly, the energies of X_1 are slightly higher than that of monolayer. As seen from Table 4.2, the *GW* correction for AFM rhombohedral (LT) bilayer is 2.61 eV, which is about 200 meV smaller than that of the monolayer. However, the *e-h* binding energy of the bilayer is reduced by

about 300 meV than that of the monolayer. As a result, the absolute value of exciton energy is slightly increased finally. This is an opposite trend according to the usual quantum confinement effect, in which thinner samples show a blue shift of the optical spectrum [48,49,52].

In most typical semiconductors, the *e-h* binding energy is usually smaller than GW self-energy correction. As a result, even if *e-h* binding energy and self-energy correction follow a similar scaling law as the dielectric screening environment changes, the reduction of *e-h* binding energy is smaller than that of the self-energy correction, resulting in a normal quantum confinement effect (the "optical gap" is reduced for thicker samples).

However, in $CrCl_3$, the quasiparticle energy correction is less than the *e-h* binding energy for all studied structures, which results in lower "optical gaps" than DFT band gaps. Therefore, for thicker samples, the reduction of *e-h* binding energy is also larger than that of the self-energy correction, resulting in the unusual quantum confinement effect. In this sense, the fundamental reason is the huge *e-h* binding energy. Compared with typical 2D semiconductors, in which the enhancement of excitonic effects is mainly from the reduced screening, *e-h* binding energy of 2D $CrCl_3$ is further enlarged by the flat bands with significant joint density of states (JDOS). Therefore, the unusual quantum confinement effect is essentially associated with the flat bands. For example, the similar behavior was reported in another flat band material CrI_3 [4], where the "optical gap" of bulk is also larger than that of monolayer.

Such an unusual confinement effect is due to the enhanced excitonic effects in $CrCl_3$, where *e-h* binding energy is larger than the self-energy (*GW*) correction. Following a similar scaling law as dielectric screening increases, the reduction of *e-h* binding energy in thicker samples is larger than the reduction of self-energy correction. As a competing result, the absolute energy of the X_1

exciton is slightly increased. In other words, this unusual quantum confinement effect is essentially from the flat bands with significant JDOS. This quantum confinement effect was reported in previous studies of other vdW magnetic structures [63].

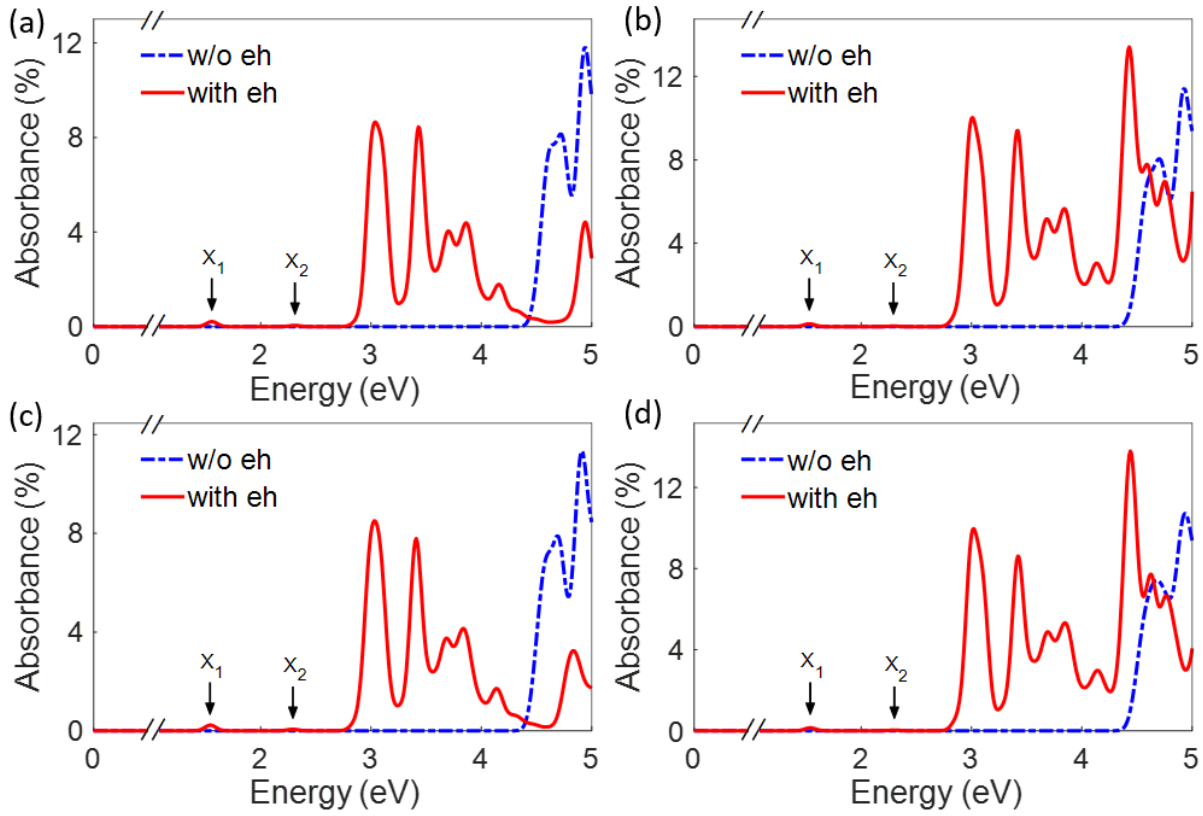

Figure 4.8 Optical absorbance of bilayer $CrCl_3$ without and with *e-h* interactions: (a) those of the LT rhombohedral stacking with an AFM interlayer coupling; (b) those of the LT rhombohedral stacking with a FM interlayer coupling; (c) those of the HT monoclinic stacking with an AFM interlayer coupling; (d) those of the HT monoclinic stacking with a FM interlayer coupling. The two characteristic excitonic peaks are marked as X_1 and X_2, respectively.

Table 4.2 Summary of DFT and *GW* band gaps (the values listed are for the direct band gap, and the values in the parenthesis are for the indirect band gap), X_1 and X_2 exciton energy and their experimental values for monolayer, bilayer and bulk $CrCl_3$. The unit is eV.

		DFT band gap	*GW* band gap	X_1 energy	X_1 energy expt.	X_2 energy	X_2 energy expt.
Monolayer		1.87 (1.84)	4.69 (4.66)	1.48	~ 1.43 (PL) [66]	2.25	_
2L	Rhombohedral AFM	1.87 (1.84)	4.48 (4.45)	1.55	_	2.31	_
	Rhombohedral FM	1.83 (1.80)	4.43 (4.40)	1.53	_	2.29	_
	Monoclinic AFM	1.85 (1.84)	4.44 (4.43)	1.54	_	2.29	_
	Monoclinic FM	1.81 (1.80)	4.41 (4.40)	1.53	_	2.30	_
bulk	Rhombohedral AFM (in-plane polarization)	1.87 (1.85)	3.89 (3.87)	1.78	~ 1.7 (Abs) [19,48]	2.51	~ 2.3 (Abs) [19,48]

4.5 Bulk $CrCl_3$

We have performed the *GW*-BSE calculations on bulk $CrCl_3$. Given the results from bilayer $CrCl_3$ where quasiparticle energy corrections and absorption spectra are not sensitive to the interlayer stacking and magnetic order, we only consider the experimentally observed rhombohedral bulk structure with the AFM interlayer coupling [19]. The DFT-calculated band structure of bulk $CrCl_3$ is presented in Figure 4.9 (a). Interestingly, quantum confinement effects are nearly negligible within DFT results: the band structure and band gap of bulk $CrCl_3$ is nearly the same as those of monolayer and bilayer structures.

The *GW*-calculated QP energy vs the DFT results are summarized in Table 4.2. Significant self-energy corrections are observed in bulk $CrCl_3$. Because of stronger screening in three

dimensions, the *GW* enlargement of the band gap is around 2.0 eV, and it is smaller than those in the monolayer (around 2.8 eV) and bilayer (around 2.6 eV). Nonetheless, this reduction of band gap from the monolayer (~ 4.66 eV) to bulk (~ 3.87 eV) is significantly smaller than other typical semiconductors such as black phosphorous (~ 2 eV in the monolayer and less than 0.3 eV in bulk) [48] and tellurium (~ 2.35 eV in the monolayer and less than 0.41 eV in bulk) [52].

Further we have calculated the absorption spectrum $\varepsilon_2(\omega)$ of bulk $CrCl_3$. Because the depolarization effect is negligible in bulk structures, we consider both in-plane and out-of-plane polarizations of incident light, as shown in Figures 4.9 (b) and 4.9 (c), respectively. As expected, before including *e-h* interactions, both the optical absorption spectra start from the QP band gap around 3.9 eV. Excitonic effects substantially shift the main optical absorption spectrum to between 3 and 4 eV. For in-plane polarized incident light [Figure 4.9 (b)], those two characteristic excitonic peaks (X_1 and X_2) are similar to the monolayer and bilayer cases and are located at 1.78 and 2.51 eV with *e-h* binding energies of 2.11 and 1.38 eV, respectively. These exciton energies are higher than those of the bilayer (1.55 and 2.31 eV) and monolayer (1.48 and 2.25 eV), exhibiting an opposite trend of the usual quantum confinement effects according to the same reason as explained in the Chap. 4.4 for bilayer $CrCl_3$. Moreover, the dipole oscillator strength of these two characteristic peaks is also enhanced. This can be from the stronger interlayer hybridization that enhances the overlap of electron and hole wave functions and corresponding transition matrices.

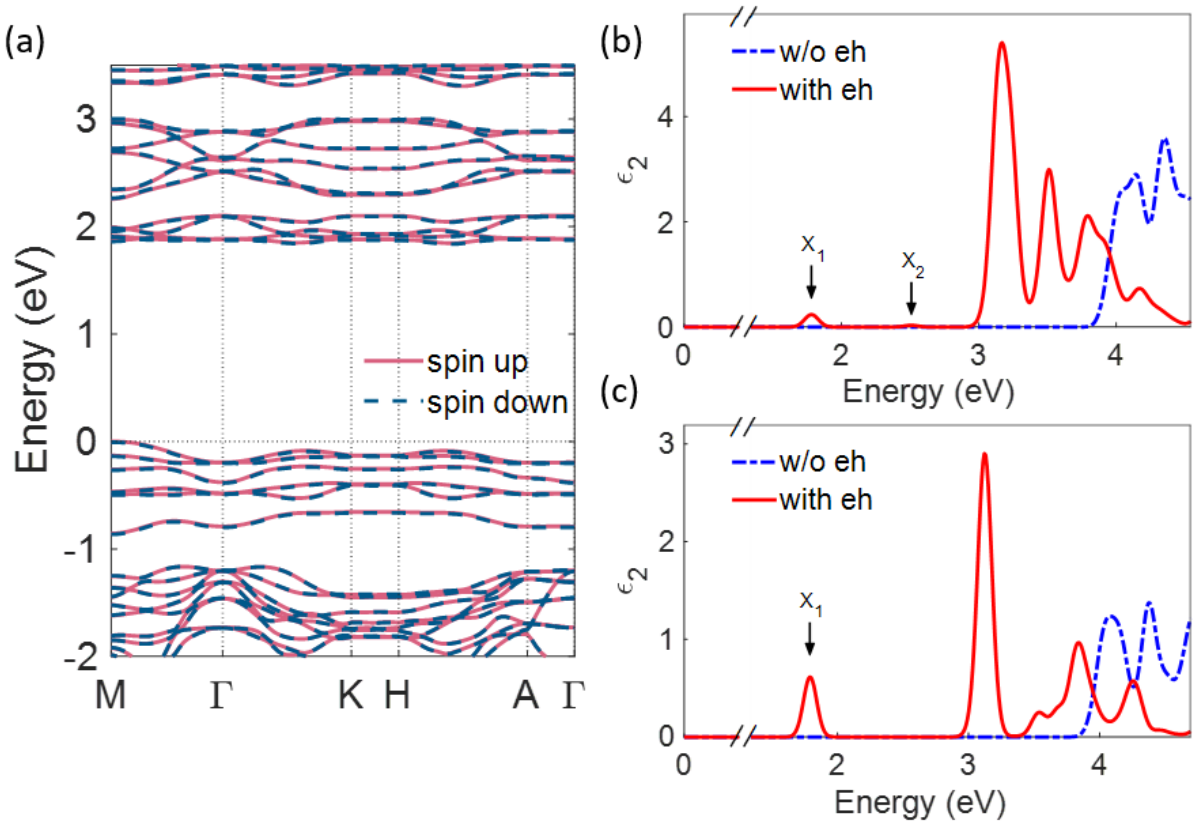

Figure 4.9 Electronic and optical properties of bulk $CrCl_3$ in the LT rhombohedral stacking with an AFM interlayer coupling: (a) the DFT-calculated band structure. The energy of the valence band maximum is set to be zero. The optical absorption spectra without and with *e-h* interactions for incident light polarized in the (b) in-plane and (c) out-of-plane direction.

The dipole oscillator strength distribution is largely different for different incident-light polarizations, resulting in a highly anisotropic optical spectrum. For incident light polarized along the out-of-plane direction [Figure 4.9 (c)], the characteristic peak X_2 becomes optically dark, and the dipole oscillator strength of X_1 is further enhanced. In addition, the main absorption between 3 eV and 4 eV develops into more isolated absorption peaks around 3.1 and 3.8 eV. The

redistribution of exciton dipole oscillator strength under different incident light polarization may be employed in experiments to detect the crystal orientation.

There are extensive experiments on the absorption spectrum of bulk $CrCl_3$, as summarized in Table 4.2. In Refs. [19,48], they reported absorption peaks around 1.7 and 2.3 eV for bulk $CrCl_3$. These are in good accordance with our calculated absorption peaks at 1.78 eV (X_1) and 2.51 eV (X_2) and their energy splitting (0.73 eV). It has to be pointed out that the measurements of Ref. [48] were performed at 80 and 300 K, which are above the Néel temperature (14 K) of bulk $CrCl_3$. It could be a problem to compare our results under a perfect AFM order to measurements of the paramagnetic order. Unfortunately, we cannot find optical measurements of bulk $CrCl_3$ under its Néel temperature. On the other hand, there is a report of another A-type AFM material $CrPS_4$, in which the photoluminescence peak positions are not shifted when passing the Néel temperature [83], although the peak width and shape change as temperature increases. Therefore, we expect that those absorption peaks in Refs. [57,82] will not be substantially changed by the magnetic order.

4.6 Evolution of band gaps and excitons with dimensionality

Finally, we have summarized the evolution of band gaps and characteristic excitons of $CrCl_3$ from monolayer, bilayer, to bulk. Given available measurements and the insensitivity of electronic and optical properties to the interlayer stacking and magnetic configurations, we use the results of interlayer LT structures and AFM coupling, and the fitting results are universal for all configurations. In Figure 4.10 (a), the evolution of the DFT and QP band gaps as well as the

"optical gap" (the first bright exciton peak X_1) is presented. To quantitatively provide the band gap dependence on the layer number, we employ the widely used empirical power law formula [48,49,84]:

$$E^N = E^{\infty}_{bulk} + \frac{A}{N^{\alpha}}, \tag{4.6}$$

where N is the layer number and E^{∞}_{bulk} represents the bulk value. The fitted results are included in Table 4.3. Although the DFT band gap barely changes from monolayer to bulk, the significant QP energy corrections reflect the trend of the increased dielectric screening effect. The failure of DFT in predicting the band gap as well as the dielectric screening effect indicates it is important to go beyond DFT in calculating the electronic properties of vdW layered magnetic materials even for obtaining qualitative trends of quantum confinement. Interestingly, the *GW*-calculated band gap follows the $1/N^{0.5}$ power law. This decay is slower than the usual quantum confinement case with $1/N^2$ [84] based on free-electron gas, and indicates that many-electron correlations are significantly less sensitive to the quantum confinement in correlated $CrCl_3$.

Table 4.3 Fitting parameters of DFT, QP band gaps, and "optical gap" (energy of the first bright exciton X_1) to the layer number according to the power law formula $E^{\infty}_{bulk} + A/N^{\alpha}$.

	DFT	QP	"Optical gap"
α	0.03	0.51	0.48
A	-0.01	0.79	-0.30

In Figure 4.10 (b), we focus on those two characteristic peaks (X_1 and X_2). As noticed in above presentations, the brightness of these two excitons are sensitive to the layer number of structures. As shown in Figure 4.10 (b), the absorbance of the lower-energy exciton (X_1) is more sensitive to the thickness, and it is increased from 0.06% in monolayer to 0.25% in bulk. Thus, we expect these two characteristic excitons can be useful to estimate the thickness of samples.

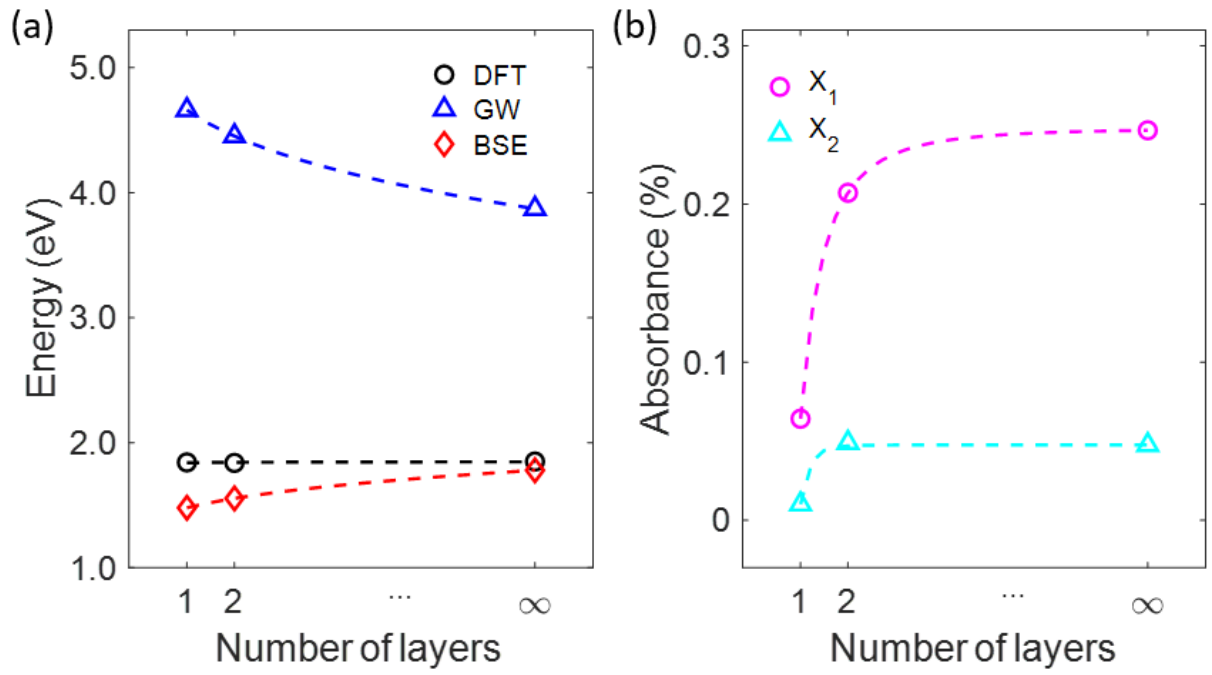

Figure 4.10 (a) Evolution of DFT, QP band gaps and "optical gap" (energy of the first bright exciton X_1) of $CrCl_3$ with the layer number. The dashed lines are power law fits to the results. (b) Evolution of the optical absorbance of the characteristic peaks X_1 and X_2 with the layer number.

4.7 Conclusions

In summary, we have systematically studied the electronic and optical properties from monolayer, bilayer to bulk $CrCl_3$ using a first-principles MBPT approach. Unlike typical

semiconductors, the increased dielectric screening in bulk $CrCl_3$ only renders a less than 20% decrease in the QP band gap relative to the monolayer case, and the energy of the lowest bright exciton is even slightly increased from monolayer to bulk. Besides, the absorption spectrum of bulk $CrCl_3$ resembles that of the monolayer, with significant *e-h* binding energy of the lowest exciton state around 2 eV compared with 3 eV in monolayer $CrCl_3$. The physics origin of different dipole oscillator strengths between excitons is discussed based on the interference effect between exciton wave functions and interband transition matrices. Our calculated results are in good agreement with available measurements. Finally, we find that the absorption spectra of the vdW magnet $CrCl_3$ is not sensitive to the interlayer magnetic order or stacking structure. Magneto-optical probes such as the Kerr effect and MCD may be needed in future experiments to probe the magnetic order in these magnetic materials.

Chapter 5: Moiré Potential Renormalization Induced by Quasiparticle-Plasmon Coupling

5.1 Introduction

Moiré potential profile can form flat electronic bands and manifest novel correlated states of electrons, where carrier doping is essential for observing those correlations. In this work, we uncover a hidden but remarkable many-electron effect: doped carriers form a two-dimensional plasmon and strongly couple with quasiparticles to renormalize moiré potential and realize ultra-flat bands. Using many-body perturbation theory, we demonstrate this effect in twisted MoS_2/WS_2 heterobilayer. The moiré potential is significantly enhanced upon carrier doping, and the bandwidth is reduced by an order of magnitude, leading to drastic quenching of electronic kinetic energy and stronger correlation. We further predict that the competition between correlated mechanisms can be effectively controlled via doping, giving hope to a quantum transition between Mott and charge-transfer insulating states. Our work reveals that the potential renormalization effect of doping is much more significant in determining and controlling many-electron electronic correlations than sole filling-factor tuning in moiré crystals.

When two van der Waals (vdW) layers are stacked together, moiré patterns naturally form along with a lattice mismatch or twist angle between the constituent layers. Due to the intrinsic periodic potential, flat moiré bands can be formed [1], which induce complex correlated physics, such as the superconductivity and insulating states observed in twisted bilayer graphene [2,3]. Recently, twisted transition metal dichalcogenide (TMD) heterobilayers have gained increasing attention, where the layer degeneracy is natively broken, and the semiconducting nature provides

higher electrical tunability and optical accessibility [86–93]. Mott insulating and generalized Wigner crystal states were observed in half and fractionally filled TMD moiré superlattices as a result of correlated quantum physics [20,21,94–99]. Furthermore, displacement field-induced quantum anomalous Hall effect was predicted and observed in half hole-filled $MoTe_2/WSe_2$ moiré lattices due to the interlayer hybridization [100–102]. These works establish TMD heterobilayers as a versatile playground for forming flat bands and studying correlated quantum phenomena.

Gate-field tunable filling factor is essential in realizing the above correlated physics in two-dimensional (2D) moiré systems. To date, most works have adopted the assumption that doped carriers effectively tune the filling factor while not affect quasiparticle (QP) energies and hence the moiré potential. However, doped carriers will inevitably alter the electronic screening, which is known important in determining the strong many-electron interactions and QP energies in 2D structures [103–107]. Besides, moiré potential will naturally induce inhomogeneous carrier distributions within moiré superlattices. As a result, inhomogeneous many-electron effects are expected, which may substantially revise the moiré potential, the dispersion (kinetic energy) of electronic bands, and the subsequent correlated physics pictures.

In this work, we employ first-principles many-body perturbation theory (MBPT) to study the renormalization of moiré potential under carrier doping. Figure 5.1 (a) schematically shows the doping effects on quasielectron moiré potential and wavefunctions. Because of inhomogeneous carrier distributions, the doped area will experience lowered QP potential via QP-plasmon renormalization [106–109]. Thus, the moiré potential minimum further deepens, and the quasielectron wavefunction becomes more localized in the case of carrier occupation, quenching the electronic kinetic energy and forming ultra-flat bands. We take twisted MoS_2/WS_2

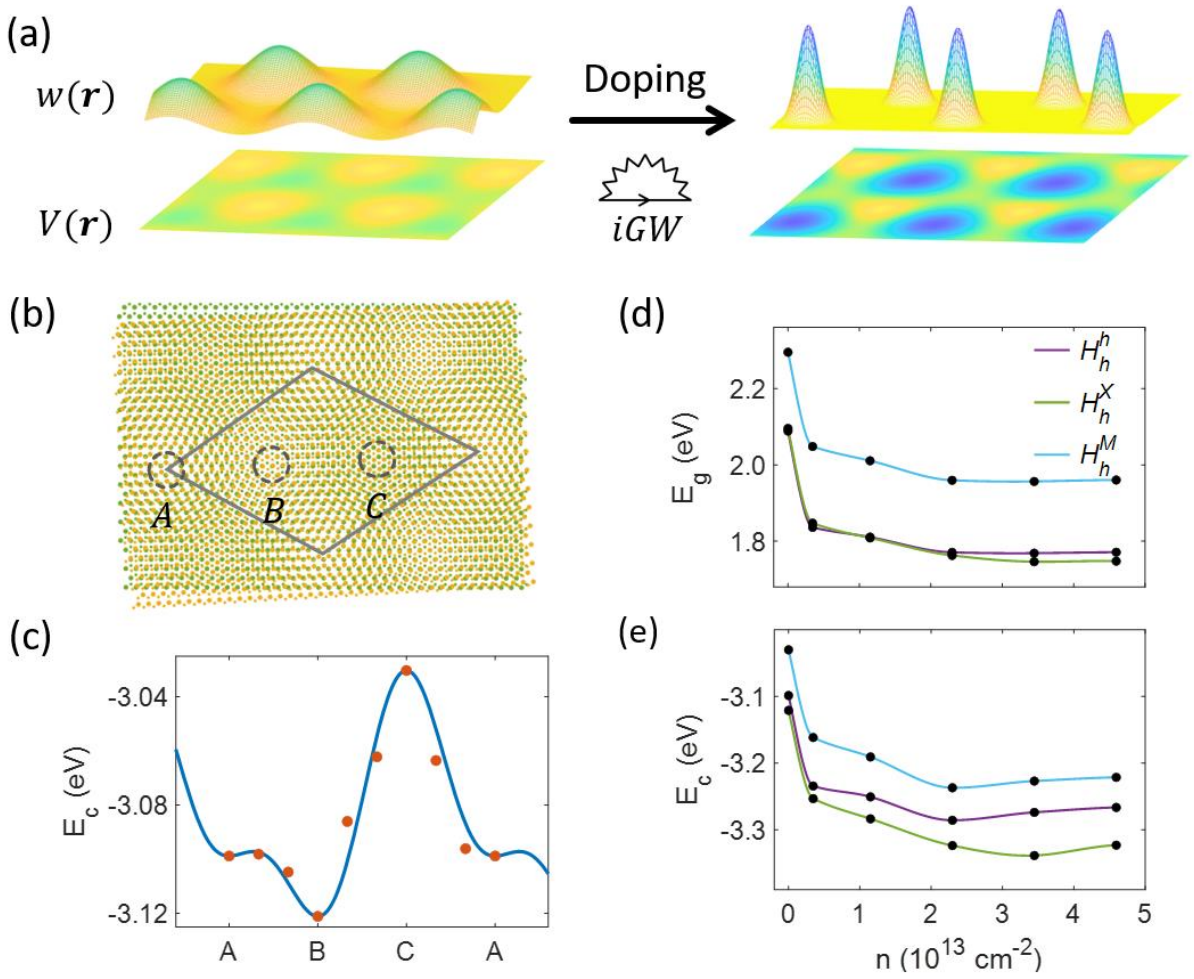

Figure 5.1 Carrier plasmon induced quasiparticle energy renormalization. (a) Schematic of doping enhanced moiré potential in semiconducting vdW superlattices. $V(r)$ and $w(r)$ are the real-space moiré potential and wavefunction of quasielectrons, respectively. Under doping, the potential minimum drops due to inhomogeneous carrier distributions and QP energy renormalization. (b) Moiré superlattice formed by a twist between the H-type MoS_2/WS_2. The three high symmetry stackings H_h^h, H_h^X and H_h^M are labeled for simplicity as A, B, C, respectively. (c) Intrinsic moiré QP potential landscape along the three interlayer registries. The red dots represent first-principles GW results. (d) Band gap and (e) CBM renormalization for the three interlayer registries of H type MoS_2/WS_2 under electron doping. The dots are from many-body perturbation theory calculations.

heterobilayer as an example to illustrate the mechanism of doping enhanced quasiparticle moiré potential. Our quantitative calculations show that a moderate doping density renders an increase of the moiré potential variation from 90 meV to 300 meV and can reduce the low-energy moiré band width by an order of magnitude. Moreover, we find that doped carriers alter the characteristic potential scales (e.g., on-site Coulomb repulsion U and charge transfer gap Δ) in different ways. As a result, a quantum phase transition from Mott insulator to charge-transfer insulator is predicted as the twist angle varies. Therefore, besides the apparent filling factor control, doping will effectively modify the moiré potential and can serve as another tuning knob for achieving ultra-flat bands and correlated physics.

The ground state calculations are performed with Quantum ESPRESSO [28], and the intrinsic self-energies are obtained by BerkeleyGW [40]. The coupling between carrier plasmon and QPs are included by the generic double plasmon pole model [106,107]. We do not include spin-orbit coupling, which does not significantly change self-energy corrections in TMDs and can be estimated by a rigid shift to QP energies [110,111]. In this work, we limit our discussions within single-particle properties. Optical properties associated with two-particle excitations, such as excitons, are not discussed but worthy of future studies.

5.2 Computational methods

The ground state properties of the MoS_2/WS_2 heterobilayer are calculated by density functional theory (DFT) within the general gradient approximation (GGA) using the Perdew-Burke-Ernzerhof (PBE) exchange-correlation functional as implemented in Quantum ESPRESSO package [28]. A $36 \times 36 \times 1$ k-grid is adopted, and the van der Waals (vdW) interactions are

included via the semiempirical Grimme-D3 scheme [112]. The plane-wave energy cutoff is 65 Ry. The vacuum distance between adjacent layers is set to be 18 Å. The many-body perturbation theory (MBPT) calculations for intrinsic structures are performed with BerkeleyGW [40]. The intrinsic quasiparticle (QP) energies are calculated by using the single-shot G_0W_0 approximation including the slab Coulomb truncation. The energy cutoff for the dielectric matrix is 10 Ry, and 224 unoccupied bands are used for the summation. For the calculation of plasmon energies, a dense k-grid of $90 \times 90 \times 1$ is used. An energy cutoff of 2 Ry and 34 unoccupied bands are sufficient to get converged plasmon frequencies. All parameters are tested for QP energy convergence within 50 meV.

When filling electrons in the conduction band minimum (CBM) moiré potential, we sweep the Fermi energy and determine the local doping density by the energy difference between the Fermi energy and the local potential. The Fermi energy is chosen when the integrated doping density over the moiré superlattice is within 1% difference with the number of doped electrons. Then the renormalized moiré potential is determined by the CBM renormalization at local doping density as in Figure 5.1 (e). We self-consistently run the potential renormalization process until convergence is reached (i.e. the Fermi level variation between two consecutive steps is less than 1 meV).

5.3 Quasiparticle band renormalization

Figure 5.1 (b) shows the moiré superlattices formed by a twist between the H stacked MoS_2/WS_2 bilayers. Three distinct high symmetry stacking orders H_h^h, H_h^X and H_h^M can be recognized (labeled for simplicity as A, B, C in Figure 5.1 (b), respectively), where the superscripts

represent a hollow/chalcogen/metal atom center in the top layer that is vertically aligned with a hollow center in the bottom layer, respectively. The atomic structures of the three local registries are shown in Figure 5.2 (a), and the quasiparticle band structure for the H_h^h stacking is shown in Figure 5.2 (b). The corresponding results for *R* stacked MoS_2/WS_2 are shown in Figure 5.3, along with the intrinsic moiré potential landscape. In the following sections, we will take the *H* stacking as an example, and the results for *R* stacking should be similar.

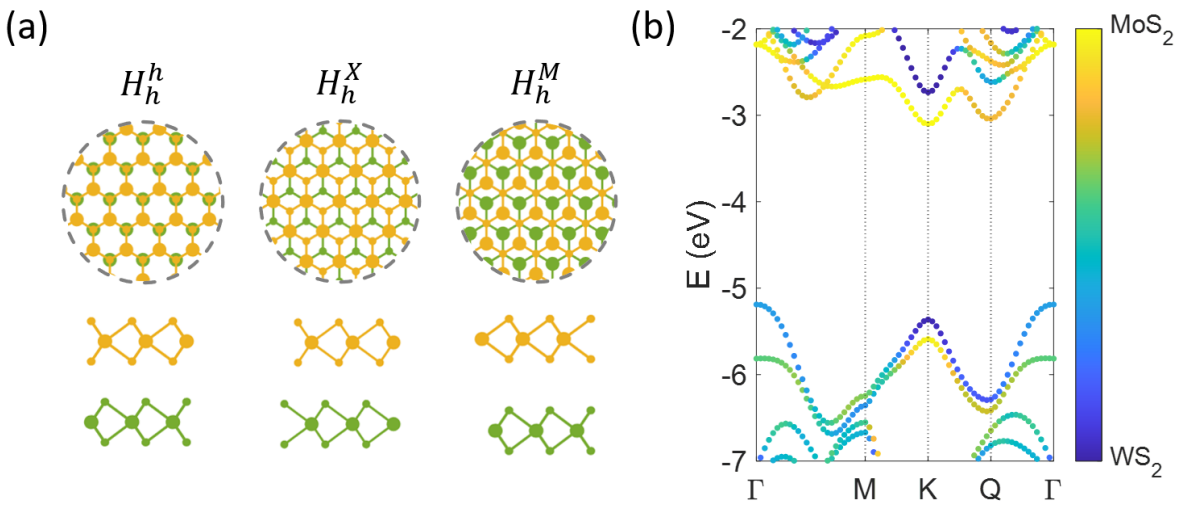

Figure 5.2 Intrinsic quasiparticle electronic structures. (a) Moiré superlattice formed by a twist between the *H*-type MoS_2/WS_2. (b) Local stacking orders of three high-symmetry interlayer registries as labeled in (a). (c) QP band structure of intrinsic H_h^h stacked MoS_2/WS_2. The energies are relative to the vacuum level. The projected layer components are represented by the color bar.

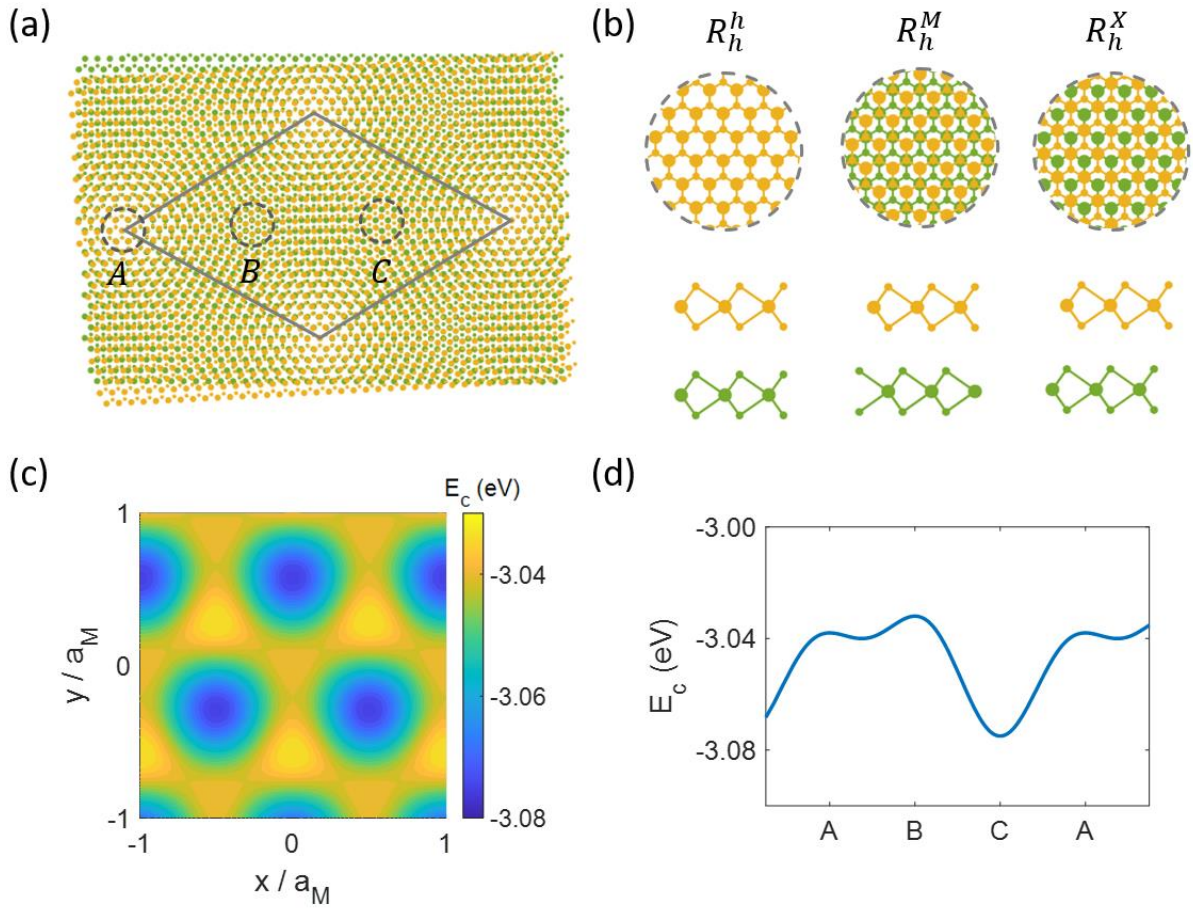

Figure 5.3 Intrinsic moiré potential of *R* type heterobilayer. (a) Moiré superlattice formed by a twist between the *R* stacked MoS_2/WS_2. The three high symmetry local registries are labeled. (b) The local stacking orders (top view and side view) of the three registries as labeled in (a). (c) Real space moiré potential of the conduction band minimum in *R* stacked MoS_2/WS_2. (d) Moiré potential landscape along the three interlayer registries.

The *ab initio* QP self-energy of the three local atomic registries are calculated under the GW approximation, $\Sigma = iGW$. The CBM for three high-symmetry stackings are all at *K* point in the reciprocal space. The locally varying stackings cause a periodic modulation of the CBM energy.

Quasielectrons in the superlattice hence experience a periodic potential, which can be interpolated by a Fourier expansion over the nearest moiré reciprocal lattice vectors

$$V(\boldsymbol{r}) = E_c(\boldsymbol{r}) = T_0 + 2V_0 \sum_{i=1,2,3} \cos\left(\boldsymbol{b}_i \cdot \boldsymbol{r} \pm \psi\right),$$

(5.1)

where E_c is the local CBM. For intrinsic MoS_2/WS_2 heterobilayer, the fitted parameters (T_0, V_0, ψ) from *ab initio* MBPT are $(-3.083\ e\text{V}, 9\ me\text{V}, 14°)$. Figure 1c plots the QP moiré potential calculated by Eq. (5.1) along the three high symmetry stacking sites. It agrees well with first-principles GW results (isolated dots), and the variation of local CBM is 90 meV. This is similar to previous DFT results [88,113] since the self-energy corrections are similar for different stackings of the intrinsic heterobilayer.

Considering the effects from doped carriers, the QP self-energy can be obtained by [105–107,114]

$$\begin{aligned}\Sigma &= i(G_{int}W_{int} + \delta G W_{int} + G_{int}\delta W + \delta G \delta W) \\ &\equiv i(\Sigma_{int} + \Sigma_1 + \Sigma_2 + \Sigma_3).\end{aligned}$$

(5.2)

The subscript int denotes the operator in the intrinsic structure, and δ terms account for the doping effects. Σ_1 is only affected by the carrier occupation

$$\Sigma_1^{n\boldsymbol{k}}(E) = -\Sigma_{n',GG'} \int_{\boldsymbol{q}<k_f} \frac{d^2\boldsymbol{q}}{(2\pi)^2} \xi_{\boldsymbol{GG}'}^{nn'}(\boldsymbol{k}, -\boldsymbol{q}) W_{\text{int},\boldsymbol{GG}'}\left(\boldsymbol{q}, E - \varepsilon_{n\boldsymbol{k}-\boldsymbol{q}}\right),$$

(5.3)

where $\xi_{\boldsymbol{GG'}}^{nn'}(k,q) = M_{nn'}^{*}(\boldsymbol{k},\boldsymbol{q},\boldsymbol{G})M_{nn'}(\boldsymbol{k},\boldsymbol{q},\boldsymbol{G'})$ contains the band structure effect and $M_{nn'}(\boldsymbol{k},\boldsymbol{q},\boldsymbol{G})$ is the plane-wave matrix element. k_f is the Fermi wave vector. Σ_2 and Σ_3 have contributions from the variation of dielectric screening $\delta W = v\delta\epsilon^{-1}$, where v is the bare Coulomb interaction. The calculation of $\delta\epsilon^{-1}$ requires a description of the interaction between carrier plasmon and quasiparticles. As shown in previous works [106,107], the dynamical screening effect can be accounted for by an approximation to the head matrix elements using the carrier-plasmon pole model $\delta\epsilon_{00}^{-1}(q,\omega) = \frac{\Omega_d^2(q)}{\omega^2-\omega_d^2(q)}$, where $\Omega_d(q)$ and $\omega_d(q)$ are the plasmon-pole strength and frequency that can be obtained by first-principles calculations [106,107]. The explicit forms for Σ_2 and Σ_3 are thus

$$\Sigma_2^{n\boldsymbol{k}}(E) = \pm\int_{q<q_c}\frac{d^2\boldsymbol{q}}{(2\pi)^2}\xi_{\boldsymbol{00}}^{nn}(\boldsymbol{k},-\boldsymbol{q})\delta W_{\boldsymbol{00}}^{\pm}\left(\boldsymbol{q},E-\varepsilon_{n\boldsymbol{k}-\boldsymbol{q}}\right),$$

(5.4)

$$\Sigma_3^{n\boldsymbol{k}}(E) = -\int_{q<k_f}\frac{d^2\boldsymbol{q}}{(2\pi)^2}\xi_{\boldsymbol{00}}^{nn}(\boldsymbol{k},-\boldsymbol{q})\delta W_{\boldsymbol{00}}\left(\boldsymbol{q},E-\varepsilon_{n\boldsymbol{k}-\boldsymbol{q}}\right),$$

(5.5)

where $\pm$ in Σ_2 are for conduction and valence states, respectively. Σ_1 and Σ_3 include the effect of partial band filling, hence under electron doping, they only contribute to the conduction band energy renormalization, and are integrated to the Fermi wavevector k_f. As a result, Σ_1 roughly scales as $-\epsilon_{int}^{-1}k_f$ and Σ_3 scales as $-\delta\epsilon^{-1}k_f$. Σ_2, on the other hand, is related to the carrier screening, and contribute to the energy renormalization of both valence and conduction bands.

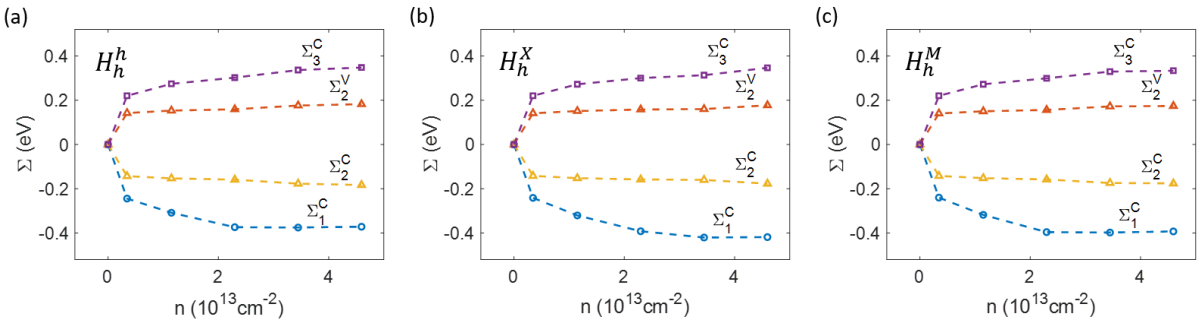

Figure 5.4 Self-energy contributions to quasiparticle energy renormalizations. Individual self-energy contributions to quasiparticle band gap renormalization for (a) H_h^h (b) H_h^X (c) H_h^M local stacking orders at different doping densities. The dots are from many-body perturbation theory calculations, and the lines are interpolations.

Under the linear response theory, we integrate Σ_2 up to a cutoff wavevector $q_c = 0.16\,\boldsymbol{b}$ for converged self-energies in the studied heterobilayer. The individual contributions of Σ_1, Σ_2, and Σ_3 to the on-shell QP self-energies are shown in Figure 5.4.

The QP self-energy under a self-consistent GW calculation is obtained by a rigid shift of the whole resonance profile so that the on-shell energy of Σ coincides with the QP solution [106,107]. Figures 5.1 (d) and (e) show the band gap and CBM renormalization for the three high-symmetry registries under doping, respectively. The results for valence band maximum are listed in Figure 5.5. As manifested by Figure 5.1 (d), the band gap renormalization (BGR) is most prominent in the light-doping side and gradually saturates to around 300 meV for all three stackings at high doping densities $\sim 2.3 \times 10^{13}$ cm^{-2}. Compared to monolayer MoS_2, whose BGR reaches about 500 meV at doping density $\sim 6.0 \times 10^{13}$ cm^{-2} [107], the band-gap reduction in heteobilayer is smaller and saturates faster. The origin of this difference is twofold. First, the intrinsic dielectric screening in a bilayer is stronger than that in a monolayer, as a

result, the extra screening introduced by the doped carriers $\Sigma_2 = iG_{int}\delta W$ is weaker. Second, the CBM of the heterobilayer features a hybridized Q point along the $\Gamma - K$ high symmetry line, which lies ~100 meV above the K point [see Figure 5.2 (b)]. As doping density increases, the Q point also gets occupied, thus the carrier-occupation effect $\Sigma_1^{CBM} = i\delta GW_{int}$ at K diminishes. In this regime, the carrier screening becomes the dominant mechanism of band renormalization. This effect is more evident in the evolution of CBM shown in Figure 5.1 (e). At low doping densities, the CBM drops dramatically, and after the onset of filling at Q, the CBM saturates with a slight uprise. The uprise is due to the transition from a holelike resonance to an electronlike resonance of $\Sigma_2^{CBM} + \Sigma_3^{CBM}$ [106] and the saturation of Σ_1^{CBM}. Note that the onset of Q occupation happens at $\sim 2.3 \times 10^{13}$ cm^{-2} for H_h^h and H_h^M stackings, and at $\sim 3.4 \times 10^{13}$ cm^{-2} for H_h^X owing to their distinct K and Q energy difference. These two factors together cause the reduced BGR in heterobilayer and its facilitated saturation behavior.

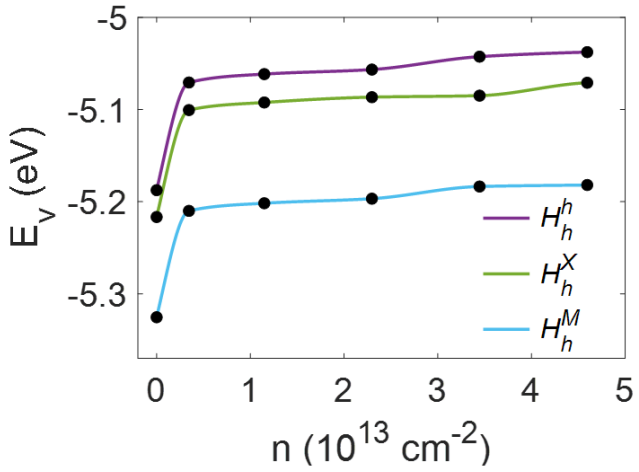

Figure 5.5 Carrier induced valence band renormalization. Valence band renormalization under electron doping for the three atomic registries. The dots are from first principles calculations, and the solid lines are fitted results.

5.4 Moiré potential landscape renormalization and ultra-flat bands

Under electron doping, the variation of the CBM at different local stackings renders an inhomogeneous carrier density within superlattices, which further modifies the moiré potential landscape according to the doping dependent band renormalization [see Figure 5.1 (e)]. We find out the doping modulated moiré potential by firstly filling electrons into the intrinsic heterobilayer potential landscape [Figure 5.1 (c)]. Then we self-consistently update the quasielectron moiré potential according to the CBM renormalization at local electron densities. The typical iteration number for convergence is about 8∼10.

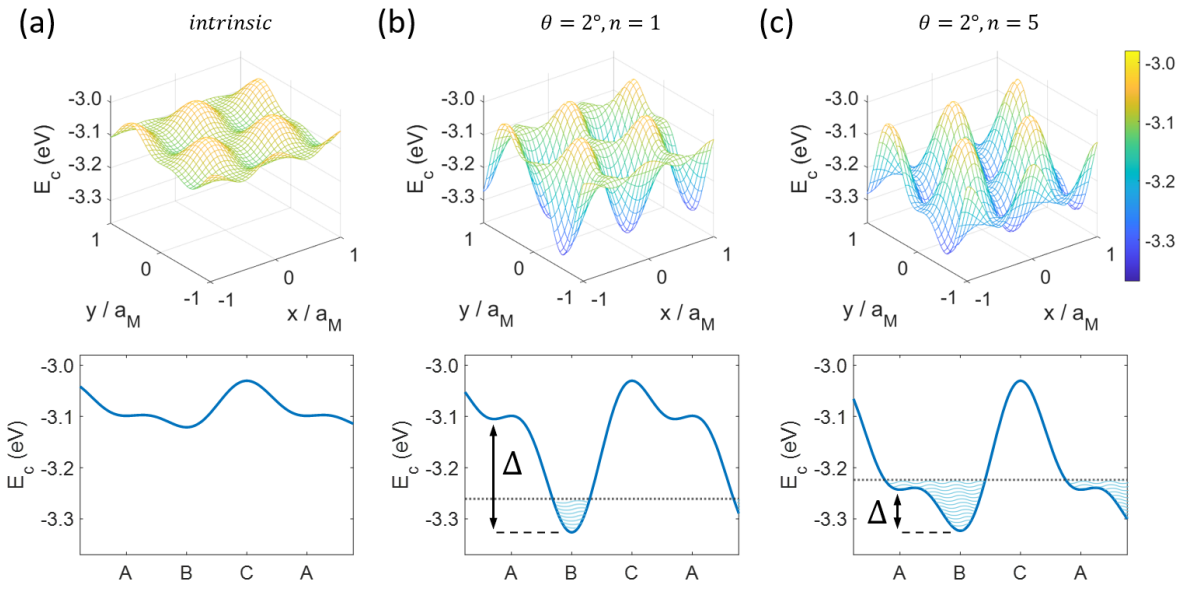

Figure 5.6 Moiré potential renormalization under carrier doping. Real-space moiré potential of the 2° twisted MoS_2/WS_2 (a) intrinsic structure (b) doped with $n = 1$ electron per moiré

superlattice (c) doped with $n = 5$ electrons per moiré superlattice. The charge-transfer gap Δ is labeled in (b) and (c).

The moiré potentials of intrinsic and doping renormalized MoS_2/WS_2 heterobilayer at 2° twist angle are presented in Figure 5.6. The overall moiré potential variation increases from around 90 meV in the intrinsic structure and saturates to over 300 meV under a moderate doping density ($\sim 1.3 \times 10^{12}$ cm^{-2} or half-filling $n = 1$ electron per moiré supercell). The dramatic change in the potential landscape is accompanied by an alteration of the moiré bands. The moiré band structures can be obtained by solving the moiré band Hamiltonian under the continuum model [113,115],

$$\mathcal{H} = \frac{\hbar^2 \boldsymbol{Q}^2}{2m} + V(\boldsymbol{r}) \quad , \tag{5.6}$$

where the moiré potential $V(\boldsymbol{r})$ as defined in Eq. (5.1) now includes the doping renormalization effect. Figures 5.7 (a) and (b) present the moiré band structures at a 2° twist angle for intrinsic and half-filled superlattices, respectively. The bandwidth of the lowest conduction band shrinks from 5 meV to 0.04 meV and becomes extremely flat under doping. The ultra-flat bands will affect a wide range of transport and optical properties, such as quenched electric conductivity due to heavy effective mass and strong excitonic effects via the enhanced van Hove singularities.

Meanwhile, the vanishing bandwidth indicates very weak inter-moiré-cell hoppings, pushing the system to the strong-correlated limit. Particularly, the lowest-energy flat band is isolated from the second mini band by 70 meV, while in the intrinsic structure, this energy separation is only

10 meV. As a result, the doping enhanced moiré potential not only flattens the bands but also isolates them, so that the flat bands are more robust to external perturbations and accessible in experiments.

We further plot the real-space wavefunctions of the low-energy moiré bands in Figures 5.7 (c) and (d). Consistent with a flat-band picture, the wavefunctions of the doped system show a much more concentrated structure. Specifically, the *s* orbital band I wavefunction is highly localized at the potential minimum (H_h^X site), whereas the wavefunction smears over adjacent potential minima in the intrinsic structure. Interestingly, the wavefunctions of the degenerate bands II and III show orthogonal symmetric *p* orbital characters as an isolated "atom". While in the intrinsic case, the wavefunctions of the non-degenerate bands II and III are not symmetric. Therefore, due to the enhanced moiré potential, the electronic states in a doped system resemble large wavelength artificial atomic arrays. Besides, since the energy separation between the lowest flat minibands are large, the trapped periodic "cold atoms" can be stable even under room temperature.

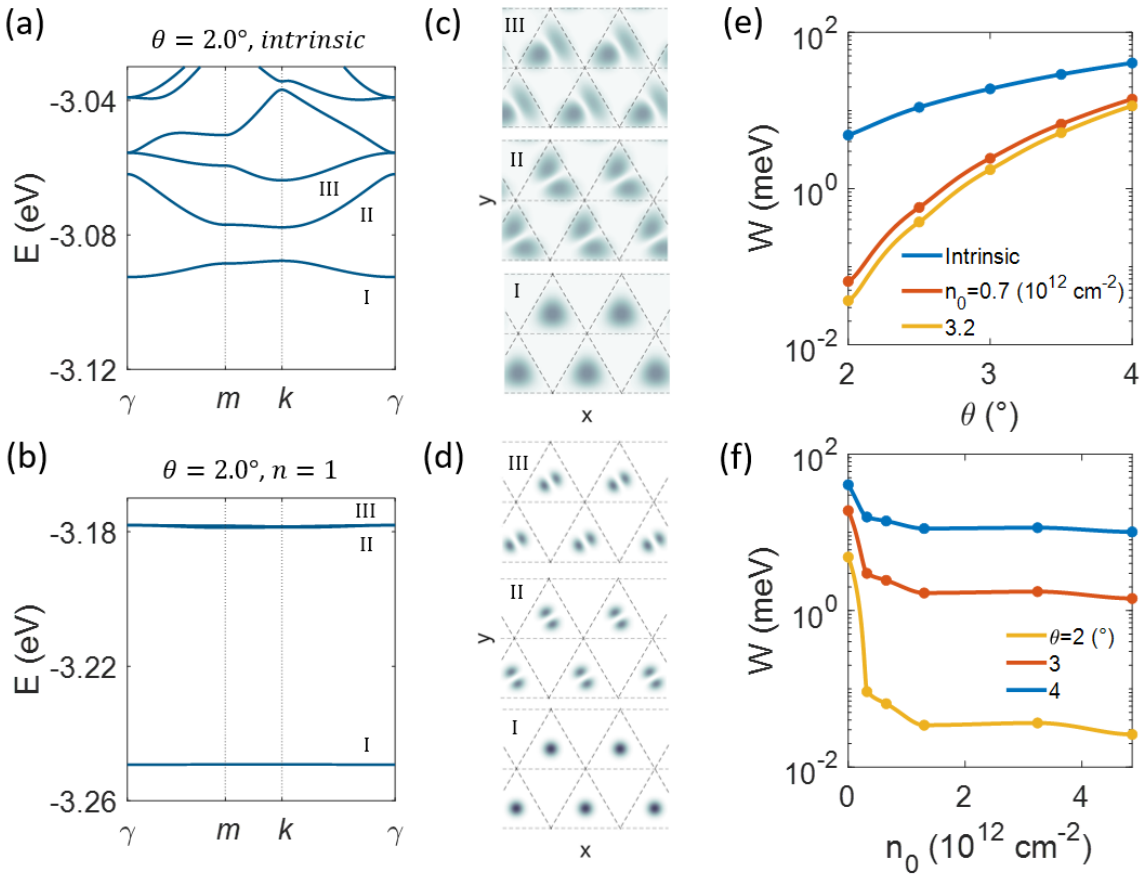

Figure 5.7 Isolated ultra-flat bands in doped moiré system. Low-energy moiré QP band structure of 2° twisted MoS_2/WS_2 (a) intrinsic structure (b) doped with $n = 1$ electron per moiré superlattice. (c) and (d) Real-space wavefunctions associated with the three lowest conduction bands I, II and III shown in (a) and (b), respectively. (e) Variation of bandwidth in terms of the twist angle. (f) Variation of bandwidth in terms of the average doping density. The vertical axes in (c) and (f) are shown in log scale for clarity.

In Figures 5.7 (e) and (f), we summarize the band I width as functions of twist angle θ and average doping density n_0, respectively. The shrinkage of bandwidth is significant at low doping

density. As shown in Figure 5.7 (e), the bandwidth shrinks from around 40 meV to 5 meV as the twist angle varies from 4° to 2° in the intrinsic structure, whereas the bandwidth reaches less than 1 meV under 2.5° at slight doping $n_0 = 0.7 \times 10^{12}$ cm^{-2}. The correlated physics hence is reachable in a larger range of twist angles in the doped system. Moreover, the moiré bandwidth experiences a dramatic decrease under slight carrier doping and becomes an order smaller than the intrinsic structure for 2° and 3° twist angles [see Figure 5.7 (f)]. This is in accordance with Figure 5.6, where the overall potential variation increases significantly at low doping density and saturates with further doping.

It is worth justifying the validity of continuum model with our many-body calculations. First, within our studied doping density range, the quasielectron-plasmon interaction range can be estimated by the characteristic scale $2k_f$ [107], which is about $0.1\,\boldsymbol{b}$. Hence the real space extent of the doping altered dielectric screening is about 10 unit cells (~3 nm), which is smaller than the studied moiré superlattices (~ 10 nm for a 2° twist angle). Second, the Wannier extent of the *s* orbitals of the localized electrons in real space can be approximated by a harmonic expansion of $V(\boldsymbol{r})$ around the potential minimum $a_W = (\hbar^2/16\pi^2 m V_0)^{1/4}\sqrt{a_M}$ [113,116]. At 2° twist angle and $n = 1$ doping, $a_W = 1.2\,n\text{m}$, which is significantly smaller than the moiré lattice constant and consistent with a flattened-band picture as shown in Figures 5.7 (a) – (d). Thus, our many-body treatment of the local dielectric screening under carrier doping shall be valid within the studied small twist angles (up to 4°).

5.5 Phase transition between Mott and charge-transfer insulators

The substantial renormalization of moiré potential by doped carriers will impact and alter a broad range of properties. Here we take the discussion of Mott and charge-transfer insulating states as an example, which is crucial for realizing unusual superconductivity. Despite the insulating states observed in doped 2D moiré crystals, the nature of these insulating states is still in controversy [116,117]. Particularly, for the moiré potential with multiple minima, the formation of insulating states can have two origins. When the local Coulomb interaction U is smaller than the potential difference Δ between minima, the ground insulating state is a Mott insulator. On the other hand, if $U > \Delta$, it is a charge-transfer insulator. In TMD heterostructures, the on-site Coulomb interaction is typically on the order of hundreds of meV, while the DFT-calculated charge-transfer energy (Δ) is generally on the order of tens of meV [113,116]. In this regard, the TMD heterostructures are normally within the charge-transfer picture. However, the many-body doping effect may change this picture.

The half-filling doping significantly increases the charge transfer energy from 22 meV [Figure 5.6 (a)] to 228 meV [Figure 5.6 (b)] for 2° twisted MoS_2/WS_2 heterobilayer. Meanwhile, the local Coulomb interaction U can be estimated by $U = e^2/4\sqrt{2\pi}\epsilon a_W$ [113], where ϵ is the average dielectric constant related to the heterobilayer entities and substrate environment. The variation of U and Δ with twist angle are summarized in Figures 5.8 (a) and (b) for half-filling $n = 1$ at $\epsilon = 7$ and 10, respectively. For $\epsilon = 7$ [Figure 5.8 (a)], a quantum phase transition between Mott and charge-transfer insulating states happens at around 2.5° as twist angle increases. At small twist angle (*i.e.*, small average doping density under the same filling factor), Δ exceeds U due to the enhanced moiré potential and charge-transfer energy as shown in Figure

5.6 (b). Therefore, the system is in the Mott-insulating state. At larger twist angle, U increases more rapidly and exceeds Δ, the system transits to a charge-transfer state. The phase transition happens at larger twist angle for higher dielectric constant. When $\epsilon = 10$ [Figure 5.8 (b)], as twist angle increases, the average doping density at half filling increases because of smaller supercell size. As shown in Figure 5.6 (c), the second potential minimum starts to get occupied, and the charge-transfer barrier Δ is reduced. The system hence transits back to a charge-transfer-like state around the twist angle of 4.1°. Therefore, the experimentally observed insulating states at half and fractional fillings can have different origins depending on the average doping density (or twisting angle) and dielectric environment. The overall phase diagram between Mott and charge-transfer insulators at half filling

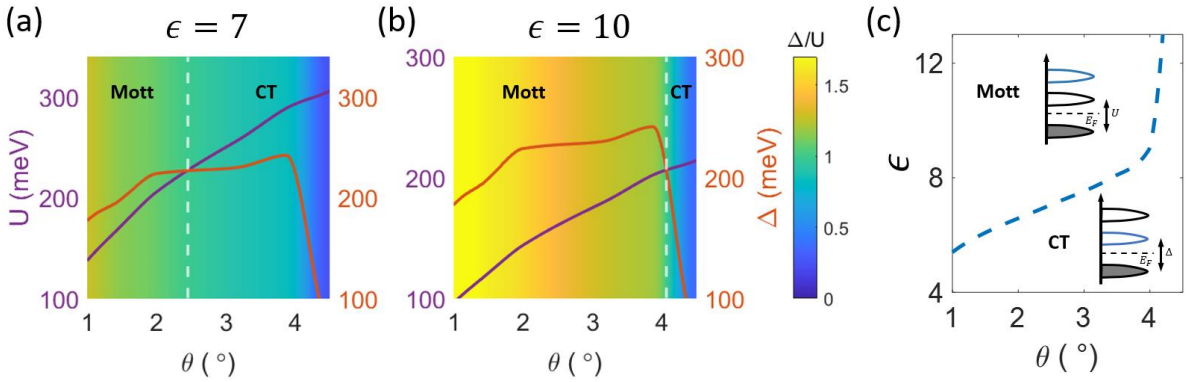

Figure 5.8 Phase diagram of the half-filled heterobilayer. Characteristic energies of U and Δ at half filling over different twist angles for (a) $\epsilon = 7$ (b) $\epsilon = 10$. The purple line is for U, and the red line is for Δ. The background represents the ratio Δ/U. The white dashed line represents the crossing between U and Δ, which is the critical point of the transition between Mott (to the left of the dashed line) and charge-transfer (CT) insulators (to the right of the dashed line). (c) Phase

diagram of Mott and charge-transfer (CT) insulators at half filling under different twist angles and dielectric constants.

is summarized in Figure 5.8 (c). A larger environmental dielectric constant favors the Mott state while a larger twist angle prefers the charge-transfer insulating state.

We notice that the shear solitons at stacking domain boundaries will influence the different domain sizes [118–121]. This structural reconstruction around domain boundaries will introduce strain into the system, which will impact the QP energies and moiré potential. As shown in previous Raman measurements on twisted bilayer MoS_2 [122] and first-principles simulations of $WSe2/WS_2$ [123], the strain due to lattice reconstruction is less than 1%. This strain level will induce a change in the QP band gap in TMD of around 100 meV, and CBM/VBM individually up to 50 meV [44]. Thus, strain will quantitatively affect the carrier distribution and potential renormalization, and the straightforward many-electron calculation in such huge moiré supercell is formidable for our simulation capability. On the other hand, the fundamental picture of enhanced moiré potential illustrated here will still be valid as long as the inhomogeneous doping picture sustains and induces inhomogeneous many-electron corrections.

5.6 Conclusions

In summary, we propose electron doping as a general way to induce enhanced moiré potential and realize pursued flat bands for quenching electronic kinetic energy in twisted semiconducting vdW structures. Combining first principles many-body perturbation theory and continuum model, we show that the nonlinear band renormalization under doping significantly deepens the moiré potential minimum and results in isolated ultra-flat bands. Depending on the average

doping density, the moiré potential landscape varies, which in turn affects the charge-transfer energy Δ and may induce a quantum phase transition between Mott insulator and charge-transfer insulator at half-filling. Our findings are crucial for understanding the carrier filling dependent electronic structures in vdW superlattices, including heterobilayers and homobilayers, and predict that electrostatic doping can be an effective tool to tune electronic correlated physics.

References

[1] K. S. Novoselov et al, *Electric Field Effect in Atomically Thin Carbon Films*, **306**, 666 (2016).

[2] A. H. Castro Neto, F. Guinea, N. M. R. Peres, K. S. Novoselov, and A. K. Geim, *The Electronic Properties of Graphene*, Rev. Mod. Phys. **81**, 109 (2009).

[3] A. K. Geim and K. S. Novoselov, *The Rise of Graphene PROGRESS*, Nat. Mater. **6**, 183 (2007).

[4] K. S. Novoselov, D. Jiang, F. Schedin, T. J. Booth, V. V. Khotkevich, S. V. Morozov, and A. K. Geim, *Two-Dimensional Atomic Crystals*, Proc. Natl. Acad. Sci. U. S. A. **102**, 10451 (2005).

[5] C. T. Phare, Y. H. Daniel Lee, J. Cardenas, and M. Lipson, *Graphene Electro-Optic Modulator with 30 GHz Bandwidth*, Nat. Photonics **9**, 511 (2015).

[6] Y. Meng, S. Ye, Y. Shen, Q. Xiao, X. Fu, R. Lu, Y. Liu, and M. Gong, *Waveguide Engineering of Graphene Optoelectronics-Modulators and Polarizers*, IEEE Photonics J. **10**, 1 (2018).

[7] K. Watanabe, T. Taniguchi, and H. Kanda, *Direct-Bandgap Properties and Evidence for Ultraviolet Lasing of Hexagonal Boron Nitride Single Crystal*, Nat. Mater. **3**, 404 (2004).

[8] G. Cassabois, P. Valvin, and B. Gil, *Hexagonal Boron Nitride Is an Indirect Bandgap Semiconductor*, Nat. Photonics **10**, 262 (2016).

[9] K. Watanabe, T. Taniguchi, K. Miya, Y. Sato, K. Nakamura, T. Niiyama, and M. Taniguchi, *Hexagonal Boron Nitride as a New Ultraviolet Luminescent Material and Its Application-Fluorescence Properties of HBN Single-Crystal Powder*, Diam. Relat. Mater. **20**, 849 (2011).

[10] K. Watanabe and T. Taniguchi, *Hexagonal Boron Nitride as a New Ultraviolet Luminescent Material and Its Application*, Int. J. Appl. Ceram. Technol. **8**, 977 (2011).

[11] K. F. Mak, C. Lee, J. Hone, J. Shan, and T. F. Heinz, *Atomically Thin MoS2: A New Direct-Gap Semiconductor*, Phys. Rev. Lett. **105**, 2 (2010).

[12] D. Xiao, G. Bin Liu, W. Feng, X. Xu, and W. Yao, *Coupled Spin and Valley Physics in Monolayers of MoS 2 and Other Group-VI Dichalcogenides*, Physical Review Letters.

[13] W. Yao, D. Xiao, and Q. Niu, *Valley-Dependent Optoelectronics from Inversion Symmetry Breaking*, Physical Review B - Condensed Matter and Materials Physics.

[14] C. Gong et al., *Discovery of Intrinsic Ferromagnetism in Two-Dimensional van Der Waals Crystals*, Nature **546**, 265 (2017).

[15] N. D. Mermin and H. Wagner, *Absence of Ferromagnetism or Antiferromagnetism in One- or Two-Dimensional Isotropic Heisenberg Models*, Phys. Rev. Lett. **17**, 1133 (1966).

[16] T. Heisenberg, *Collective Electron Ferrom Agnetism*, (1937).

[17] B. Huang et al., *Layer-Dependent Ferromagnetism in a van Der Waals Crystal down to the Monolayer Limit*, Nature **546**, 270 (2017).

[18] Y. Cao et al., *Correlated Insulator Behaviour at Half-Filling in Magic-Angle Graphene Superlattices*, Nature **556**, 80 (2018).

[19] Y. Cao, V. Fatemi, S. Fang, K. Watanabe, T. Taniguchi, E. Kaxiras, and P. Jarillo-Herrero, *Unconventional Superconductivity in Magic-Angle Graphene Superlattices*, Nature **556**, 43 (2018).

[20] E. C. Regan et al., *Mott and Generalized Wigner Crystal States in WSe2/WS2 Moiré Superlattices*, Nature **579**, 359 (2020).

[21] C. Jin et al., *Stripe Phases in WSe2/WS2 Moiré Superlattices*, Nat. Mater. **20**, 940 (2021).

[22] K. Tran et al., *Evidence for Moiré Excitons in van Der Waals Heterostructures*, Nature **567**, 71 (2019).

[23] P. Hohenberg and W. Kohn, *Inhomogeneous Electron Gas*, Phys. Rev. **136**, B864 (1964).

[24] W. Kohn and L. J. Sham, *Self-Consistent Equations Including Exchange and Correlation Effects*, Phys. Rev. **140**, A1133 (1965).

[25] D. Y. Qiu, F. H. Da Jornada, and S. G. Louie, *Optical Spectrum of MoS2: Many-Body Effects and Diversity of Exciton States*, Phys. Rev. Lett. **111**, 1 (2013).

[26] M. S. Hybertsen and S. G. Louie, *Electron Correlation in Semiconductors and Insulators: Band Gaps and Quasiparticle Energies*, Phys. Rev. B (1986).

[27] M. Rohlfing and S. G. Louie, *Electron-Hole Excitations and Optical Spectra from First Principles*, Phys. Rev. B - Condens. Matter Mater. Phys. (2000).

[28] R. M. Martin, *Electronic Structure*, Vol. 21 (Cambridge University Press, 2004).

[29] R. M. Martin, L. Reining, and D. M. Ceperley, *Interacting Electrons*, Vol. 102 (Cambridge University Press, 2016).

[30] M. L. Cohen and S. G. Louie, *Fundamentals of Condensed Matter Physics*, Vol. 90 (Cambridge University Press, 2016).

[31] G. Onida, L. Reining, and A. Rubio, *Electronic Excitations: Density-Functional versus Many-Body Green's-Function Approaches*, Rev. Mod. Phys. **74**, 601 (2002).

[32] J. P. Perdew, J. A. Chevary, S. H. Vosko, K. A. Jackson, M. R. Pederson, D. J. Singh, and C. Fiolhais, *Atoms, Molecules, Solids, and Surfaces: Applications of the Generalized Gradient Approximation for Exchange and Correlation*, Phys. Rev. B **46**, 6671 (1992).

[33] A. D. Becke, *Density-Functional Exchange-Energy Approximation with Correct Asymptotic Behavior*, Phys. Rev. A **38**, 3098 (1988).

[34] J. P. Perdew, J. A. Chevary, S. H. Vosko, K. A. Jackson, M. R. Pederson, D. J. Singh, and C. Fiolhais, *Erratum: Atoms, Molecules, Solids, and Surfaces: Applications of the Generalized Gradient Approximation for Exchange and Correlation (Physical Review B (1993) 48, 7, (4978))*, Phys. Rev. B **48**, 4978 (1993).

[35] J. C. Slater, *Note on Hartree's Method [5]*, Phys. Rev. **35**, 210 (1930).

[36] W. H. Dickhoff and D. Van Neck, *Many-Body Theory Exposed!*, Vol. 17 (WORLD SCIENTIFIC, 2008).

[37] T. Mueller and E. Malic, *Exciton Physics and Device Application of Two-Dimensional Transition Metal Dichalcogenide Semiconductors*, Npj 2D Mater. Appl. **2**, 1 (2018).

[38] P. Giannozzi et al., *Advanced Capabilities for Materials Modelling with Quantum ESPRESSO*, J. Phys. Condens. Matter **29**, 465901 (2017).

[39] P. Giannozzi et al., *QUANTUM ESPRESSO: A Modular and Open-Source Software Project for Quantum Simulations of Materials*, J. Phys. Condens. Matter **21**, (2009).

[40] J. Deslippe, G. Samsonidze, D. A. Strubbe, M. Jain, M. L. Cohen, and S. G. Louie, *BerkeleyGW: A Massively Parallel Computer Package for the Calculation of the Quasiparticle and Optical Properties of Materials and Nanostructures*, Comput. Phys. Commun. (2012).

[41] K. He, N. Kumar, L. Zhao, Z. Wang, K. F. Mak, H. Zhao, and J. Shan, *Tightly Bound Excitons in Monolayer WSe2*, Phys. Rev. Lett. **113**, 1 (2014).

[42] A. Chernikov, T. C. Berkelbach, H. M. Hill, A. Rigosi, Y. Li, O. B. Aslan, D. R. Reichman, M. S. Hybertsen, and T. F. Heinz, *Exciton Binding Energy and Nonhydrogenic Rydberg Series in Monolayer WS2*, Phys. Rev. Lett. **113**, 1 (2014).

[43] A. Ramasubramaniam, *Large Excitonic Effects in Monolayers of Molybdenum and Tungsten Dichalcogenides*, Phys. Rev. B - Condens. Matter Mater. Phys. **86**, 1 (2012).

[44] W. Song and L. Yang, *Quasiparticle Band Gaps and Optical Spectra of Strained Monolayer Transition-Metal Dichalcogenides*, Phys. Rev. B **96**, 1 (2017).

[45] T. Cheiwchanchamnangij and W. R. L. Lambrecht, *Quasiparticle Band Structure Calculation of Monolayer, Bilayer, and Bulk MoS 2*, Phys. Rev. B - Condens. Matter Mater. Phys. **85**, 1 (2012).

[46] X. Wang, A. M. Jones, K. L. Seyler, V. Tran, Y. Jia, H. Zhao, H. Wang, L. Yang, X. Xu, and F. Xia, *Highly Anisotropic and Robust Excitons in Monolayer Black Phosphorus*, Nat. Nanotechnol. **10**, 517 (2015).

[47] G. Zhang, A. Chaves, S. Huang, F. Wang, Q. Xing, T. Low, and H. Yan, *Determination of Layer-Dependent Exciton Binding Energies in Few-Layer Black Phosphorus*, Sci. Adv. **4**,

1 (2018).

[48] V. Tran, R. Soklaski, Y. Liang, and L. Yang, *Layer-Controlled Band Gap and Anisotropic Excitons in Few-Layer Black Phosphorus*, Phys. Rev. B - Condens. Matter Mater. Phys. **89**, 1 (2014).

[49] V. Tran, R. Fei, and L. Yang, *Quasiparticle Energies, Excitons, and Optical Spectra of Few-Layer Black Phosphorus*, 2D Mater. **2**, 44014 (2015).

[50] N. Saigal, V. Sugunakar, and S. Ghosh, *Exciton Binding Energy in Bulk MoS2: A Reassessment*, Appl. Phys. Lett. **108**, (2016).

[51] R. Schuster, J. Trinckauf, C. Habenicht, M. Knupfer, and B. Büchner, *Anisotropic Particle-Hole Excitations in Black Phosphorus*, Phys. Rev. Lett. **115**, 1 (2015).

[52] Y. Pan, S. Gao, L. Yang, and J. Lu, *Dependence of Excited-State Properties of Tellurium on Dimensionality: From Bulk to Two Dimensions to One Dimensions*, Phys. Rev. B **98**, 1 (2018).

[53] M. L. Cohen and S. G. Louie, *Fundamentals of Condensed Matter Physics* (2016).

[54] M. W. Lin et al., *Ultrathin Nanosheets of CrSiTe3: A Semiconducting Two-Dimensional Ferromagnetic Material*, J. Mater. Chem. C (2016).

[55] C. Gong et al., *Discovery of Intrinsic Ferromagnetism in Two-Dimensional van Der Waals Crystals*, Nature (2017).

[56] B. Huang et al., *Layer-Dependent Ferromagnetism in a van Der Waals Crystal down to the Monolayer Limit*, Nature (2017).

[57] M. A. McGuire, G. Clark, S. Kc, W. M. Chance, G. E. Jellison, V. R. Cooper, X. Xu, and B. C. Sales, *Magnetic Behavior and Spin-Lattice Coupling in Cleavable van Der Waals Layered CrCl3 Crystals*, Phys. Rev. Mater. (2017).

[58] N. D. Mermin and H. Wagner, *Absence of Ferromagnetism or Antiferromagnetism in One- or Two-Dimensional Isotropic Heisenberg Models*, Phys. Rev. Lett. (1966).

[59] J. L. Lado and J. Fernández-Rossier, *On the Origin of Magnetic Anisotropy in Two Dimensional CrI3*, 2D Mater. (2017).

[60] B. Huang et al., *Electrical Control of 2D Magnetism in Bilayer CrI3*, Nat. Nanotechnol. (2018).

[61] S. Jiang, J. Shan, and K. F. Mak, *Electric-Field Switching of Two-Dimensional van Der Waals Magnets*, Nat. Mater. (2018).

[62] D. Zhong et al., *Van Der Waals Engineering of Ferromagnetic Semiconductor Heterostructures for Spin and Valleytronics*, Sci. Adv. (2017).

[63] M. Wu, Z. Li, T. Cao, and S. G. Louie, *Physical Origin of Giant Excitonic and Magneto-*

Optical Responses in Two-Dimensional Ferromagnetic Insulators, Nat. Commun. (2019).

[64] A. Molina-Sánchez, G. Catarina, D. Sangalli, and J. Fernández-Rossier, *Magneto-Optical Response of Chromium Trihalide Monolayers: Chemical Trends*.

[65] M. A. McGuire, H. Dixit, V. R. Cooper, and B. C. Sales, *Coupling of Crystal Structure and Magnetism in the Layered, Ferromagnetic Insulator Cri3*, Chem. Mater. (2015).

[66] X. Cai et al., *Atomically Thin CrCl3: An In-Plane Layered Antiferromagnetic Insulator*, Nano Lett. (2019).

[67] H. H. Kim et al., *Evolution of Interlayer and Intralayer Magnetism in Three Atomically Thin Chromium Trihalides*, Proc. Natl. Acad. Sci. U. S. A. (2019).

[68] X. Lu, R. Fei, and L. Yang, *Meron-Like Topological Spin Defects in Monolayer CrCl 3*, Arxiv (2020).

[69] Z. Sun et al., *Giant Nonreciprocal Second-Harmonic Generation from Antiferromagnetic Bilayer CrI3*, Nature.

[70] W. Song, R. Fei, and L. Yang, *Nonreciprocal Second-Harmonic Generation in Few-Layer Chromium Triiodide*, 1 (2020).

[71] J. P. Perdew, K. Burke, and M. Ernzerhof, *Generalized Gradient Approximation Made Simple*, Phys. Rev. Lett. (1996).

[72] S. Grimme, *Semiempirical GGA-Type Density Functional Constructed with a Long-Range Dispersion Correction*, J. Comput. Chem. (2006).

[73] D. R. Hamann, *Optimized Norm-Conserving Vanderbilt Pseudopotentials*, Phys. Rev. B - Condens. Matter Mater. Phys. **88**, 1 (2013).

[74] C. D. Spataru, S. Ismail-Beigi, L. X. Benedict, and S. G. Louie, *Excitonic Effects and Optical Spectra of Single-Walled Carbon Nanotubes*, Phys. Rev. Lett. (2004).

[75] L. Yang, C. D. Spataru, S. G. Louie, and M. Y. Chou, *Enhanced Electron-Hole Interaction and Optical Absorption in a Silicon Nanowire*, Phys. Rev. B - Condens. Matter Mater. Phys. (2007).

[76] M. Cococcioni and S. De Gironcoli, *Linear Response Approach to the Calculation of the Effective Interaction Parameters in the LDA+U Method*, Phys. Rev. B - Condens. Matter Mater. Phys. (2005).

[77] T. Miyake, P. Zhang, M. L. Cohen, and S. G. Louie, *Quasiparticle Energy of Semicore d Electrons in ZnS: Combined LDA+U and GW Approach*, Phys. Rev. B - Condens. Matter Mater. Phys. (2006).

[78] B. C. Shih, Y. Xue, P. Zhang, M. L. Cohen, and S. G. Louie, *Quasiparticle Band Gap of ZnO: High Accuracy from the Conventional G0W0 Approach*, Phys. Rev. Lett. (2010).

[79] L. Yang, J. Deslippe, C. H. Park, M. L. Cohen, and S. G. Louie, *Excitonic Effects on the Optical Response of Graphene and Bilayer Graphene*, Phys. Rev. Lett. (2009).

[80] D. R. Klein et al., *Enhancement of Interlayer Exchange in an Ultrathin Two-Dimensional Magnet*, Nature Physics.

[81] H. Wang, V. Eyert, and U. Schwingenschlögl, *Electronic Structure and Magnetic Ordering of the Semiconducting Chromium Trihalides CrCl3, CrBr3, and CrI3*, J. Phys. Condens. Matter (2011).

[82] R. P. Mildren, *Intrinsic Optical Properties of Diamond*, Opt. Eng. Diam. **691**, 1 (2013).

[83] P. Gu et al., *Photoluminescent Quantum Interference in a van Der Waals Magnet Preserved by Symmetry Breaking*, ACS Nano **14**, 1003 (2020).

[84] X. Zhao, C. M. Wei, L. Yang, and M. Y. Chou, *Quantum Confinement and Electronic Properties of Silicon Nanowires*, Phys. Rev. Lett. (2004).

[85] R. Bistritzer and A. H. MacDonald, *Moiré Bands in Twisted Double-Layer Graphene*, Proc. Natl. Acad. Sci. U. S. A. **108**, 12233 (2011).

[86] K. Tran et al., *Evidence for Moiré Excitons in van Der Waals Heterostructures*, Nature **567**, 71 (2019).

[87] C. Jin et al., *Observation of Moiré Excitons in WSe2/WS2 Heterostructure Superlattices*, Nature **567**, 76 (2019).

[88] H. Yu, G. Bin Liu, J. Tang, X. Xu, and W. Yao, *Moiré Excitons: From Programmable Quantum Emitter Arrays to Spin-Orbit–Coupled Artificial Lattices*, Sci. Adv. **3**, 1 (2017).

[89] Z. Li et al., *Interlayer Exciton Transport in MoSe2/WSe2Heterostructures*, ACS Nano **15**, 1539 (2021).

[90] X. Lu, X. Li, and L. Yang, *Modulated Interlayer Exciton Properties in a Two-Dimensional Moiré Crystal*, Phys. Rev. B **100**, 155416 (2019).

[91] F. Wu, T. Lovorn, and A. H. Macdonald, *Theory of Optical Absorption by Interlayer Excitons in Transition Metal Dichalcogenide Heterobilayers*, Phys. Rev. B **97**, 1 (2018).

[92] H. Baek, M. Brotons-Gisbert, Z. X. Koong, A. Campbell, M. Rambach, K. Watanabe, T. Taniguchi, and B. D. Gerardot, *Highly Energy-Tunable Quantum Light from Moiré-Trapped Excitons*, Sci. Adv. **6**, 1 (2020).

[93] T. I. Andersen et al., *Excitons in a Reconstructed Moiré Potential in Twisted WSe2/WSe2 Homobilayers*, Nat. Mater. **20**, 480 (2021).

[94] Y. Xu, S. Liu, D. A. Rhodes, K. Watanabe, T. Taniguchi, J. Hone, V. Elser, K. F. Mak, and J. Shan, *Correlated Insulating States at Fractional Fillings of Moiré Superlattices*, Nature **587**, 214 (2020).

[95] H. Li et al., *Imaging Two-Dimensional Generalized Wigner Crystals*, Nature **597**, 650 (2021).

[96] X. Huang et al., *Correlated Insulating States at Fractional Fillings of the WS2/WSe2 Moiré Lattice*, Nat. Phys. **17**, 715 (2021).

[97] Y. Tang et al., *Simulation of Hubbard Model Physics in WSe2/WS2 Moiré Superlattices*, Nature **579**, 353 (2020).

[98] T. Li et al., *Continuous Mott Transition in Semiconductor Moiré Superlattices*, Nature **597**, 350 (2021).

[99] H. Pan and S. Das Sarma, *Interaction-Driven Filling-Induced Metal-Insulator Transitions in 2D Moiré Lattices*, Physical Review Letters.

[100] Y. Zhang, T. Devakul, and L. Fu, *Spin-Textured Chern Bands in AB-Stacked Transition Metal Dichalcogenide Bilayers*, Proc. Natl. Acad. Sci. U. S. A. **118**, 2 (2021).

[101] T. Li et al., *Quantum Anomalous Hall Effect from Intertwined Moiré Bands*, Nature **600**, 641 (2021).

[102] Y. M. Xie, C. P. Zhang, J. X. Hu, K. F. Mak, and K. T. Law, *Valley-Polarized Quantum Anomalous Hall State in Moiré MoTe2/WSe2 Heterobilayers*, Phys. Rev. Lett. **128**, 1 (2022).

[103] B. Radisavljevic and A. Kis, *Mobility Engineering and a Metal-Insulator Transition in Monolayer MoS 2*, Nat. Mater. **12**, 815 (2013).

[104] S. Mouri, Y. Miyauchi, and K. Matsuda, *Tunable Photoluminescence of Monolayer MoS2 via Chemical Doping*, Nano Lett. **13**, 5944 (2013).

[105] C. D. Spataru and F. Léonard, *Quasiparticle and Exciton Renormalization Effects in Electrostatically Doped Semiconducting Carbon Nanotubes*, Chem. Phys. **413**, 81 (2013).

[106] Y. Liang and L. Yang, *Carrier Plasmon Induced Nonlinear Band Gap Renormalization in Two-Dimensional Semiconductors*, Phys. Rev. Lett. **114**, 1 (2015).

[107] S. Gao and L. Yang, *Renormalization of the Quasiparticle Band Gap in Doped Two-Dimensional Materials from Many-Body Calculations*, Phys. Rev. B **96**, 1 (2017).

[108] J. Lischner, D. Vigil-Fowler, and S. G. Louie, *Satellite Structures in the Spectral Functions of the Two-Dimensional Electron Gas in Semiconductor Quantum Wells: A GW plus Cumulant Study*, Phys. Rev. B - Condens. Matter Mater. Phys. **89**, 1 (2014).

[109] F. Caruso, H. Lambert, and F. Giustino, *Band Structures of Plasmonic Polarons*, Phys. Rev. Lett. **114**, 1 (2015).

[110] B. D. Malone and M. L. Cohen, *Quasiparticle Semiconductor Band Structures Including Spin-Orbit Interactions*, J. Phys. Condens. Matter **25**, (2013).

[111] D. Y. Qiu, F. H. Da Jornada, and S. G. Louie, *Screening and Many-Body Effects in Two-Dimensional Crystals: Monolayer MoS2*, Phys. Rev. B **93**, 1 (2016).

[112] S. Grimme, J. Antony, S. Ehrlich, and H. Krieg, *A Consistent and Accurate Ab Initio Parametrization of Density Functional Dispersion Correction (DFT-D) for the 94 Elements H-Pu*, J. Chem. Phys. **132**, (2010).

[113] F. Wu, T. Lovorn, E. Tutuc, and A. H. Macdonald, *Hubbard Model Physics in Transition Metal Dichalcogenide Moiré Bands*, Phys. Rev. Lett. **121**, 1 (2018).

[114] C. D. Spataru and F. Léonard, *Tunable Band Gaps and Excitons in Doped Semiconducting Carbon Nanotubes Made Possible by Acoustic Plasmons*, Phys. Rev. Lett. **104**, 1 (2010).

[115] J. Jung, A. Raoux, Z. Qiao, and A. H. Macdonald, *Ab Initio Theory of Moiré Superlattice Bands in Layered Two-Dimensional Materials*, Phys. Rev. B - Condens. Matter Mater. Phys. **89**, 1 (2014).

[116] Y. Zhang, N. F. Q. Yuan, and L. Fu, *Moiré Quantum Chemistry: Charge Transfer in Transition Metal Dichalcogenide Superlattices*, Phys. Rev. B **102**, 1 (2020).

[117] Y. Zhang, T. Liu, and L. Fu, *Electronic Structures, Charge Transfer, and Charge Order in Twisted Transition Metal Dichalcogenide Bilayers*, Phys. Rev. B **103**, 1 (2021).

[118] H. Li et al., *Imaging Moiré Flat Bands in Three-Dimensional Reconstructed WSe2/WS2 Superlattices*, Nat. Mater. **20**, 945 (2021).

[119] S. Shabani, D. Halbertal, W. Wu, M. Chen, S. Liu, J. Hone, W. Yao, D. N. Basov, X. Zhu, and A. N. Pasupathy, *Deep Moiré Potentials in Twisted Transition Metal Dichalcogenide Bilayers*, Nat. Phys. **17**, 720 (2021).

[120] M. H. Naik and M. Jain, *Ultraflatbands and Shear Solitons in Moiré Patterns of Twisted Bilayer Transition Metal Dichalcogenides*, Phys. Rev. Lett. **121**, 266401 (2018).

[121] J. Kim, E. Ko, J. Jo, M. Kim, H. Yoo, Y. W. Son, and H. Cheong, *Anomalous Optical Excitations from Arrays of Whirlpooled Lattice Distortions in Moiré Superlattices*, Nat. Mater. **21**, 890 (2022).

[122] J. Quan et al., *Phonon Renormalization in Reconstructed MoS2 Moiré Superlattices*, Nat. Mater. **20**, 1100 (2021).

[123] M. H. Naik et al., *Intralayer Charge-Transfer Moiré Excitons in van Der Waals Superlattices*, Nature **609**, 52 (2022).